

# Dynamics of Propagating Waves in the Olfactory Network of a Terrestrial Mollusk: An Electrical and Optical Study

D. KLEINFELD, K. R. DELANEY, M. S. FEE, J. A. FLORES, D. W. TANK, AND A. GELPERIN

*Biological Computation Research Department, AT&T Bell Laboratories, Murray Hill, New Jersey 07974; and Department of Biosciences, Simon Fraser University, Burnaby, British Columbia V5A 1S6, Canada*

## SUMMARY AND CONCLUSIONS

1. The procerebral (PC) lobe of the terrestrial mollusk *Limax maximus* contains a highly interconnected network of local olfactory interneurons that receives ipsilateral axonal projections from superior and inferior noses. This network exhibits an  $\sim 0.7$ -Hz intrinsic oscillation in its local field potential (LFP).

2. Intracellular recordings show that the lobe contains at least two classes of neurons with activity phase locked to the oscillation. Neurons in one class produce periodic bursts of spikes, followed by a period of hyperpolarization and subsequently a depolarizing afterpotential. There is a small but significant chance for a second burst to occur during the depolarizing afterpotential; this leads to a double event in the LFP. Bursting neurons constitute  $\sim 10\%$  of the neurons in the lobe.

3. Neurons in the other class fire infrequently and do not produce periodic bursts of action potentials. However, they receive strong, periodic inhibitory input during every event in the LFP. These nonbursting cells constitute the major fraction of neurons in the lobe. There is a clear correlation between the periodic burst of action potentials in the bursting neurons and the hyperpolarization seen in nonbursting neurons.

4. Optical techniques are used to image the spatially averaged transmembrane potentials in preparations stained with voltage-sensitive dyes. The results of simultaneous optical and electrical measurements show that the major part of the optical signal can be interpreted as a superposition of the intracellular signals arising from the bursting and nonbursting neurons.

5. Successive images of the entire PC lobe show waves of electrical activity that span the width of the lobe and travel its full length along a longitudinal axis. The direction of propagation in the unperturbed lobe is always from the distal to the proximal end. The wavelength varies between preparations but is on the order of the length of the preparation.

6. One-dimensional images along the longitudinal axis of the lobe are used to construct a space-time map of the optical activity, from which we calculate the absolute contribution of bursting and nonbursting neurons to the optical signal. The contribution of the intracellular signals from the two cell types appears to vary systematically across the lobe; bursting cells dominate at middle and proximal locations, and nonbursting cells dominate at distal locations.

7. The direction and form of the waves can be perturbed either by microsurgical manipulation of the preparation or by chemical modulation of its synaptic and neuronal properties. These results suggest that the direction of propagation arises from dynamic properties of the network, as opposed to an architecture with unidirectional connectivity. Further, fragments of the lobe oscillate after surgical isolation, showing that there is not a single pacemaker region in the lobe.

8. The periodic LFP occasionally exhibits rapid, double events during which the propagating wave state is seen to transiently shift to one with nearly spatially synchronized activity along the length

of the lobe. This indicates that the lobe can support a state with essentially no temporal phase gradient, as well as one with propagating waves.

9. Although details of the circuitry within the lobe are largely unknown, analogies between the dynamics reported here and theoretical understanding of excitable media suggest that the temporal phase gradient originates from a spatial gradient of excitability along the lobe. Consistent with this hypothesis is the observation that surgically isolated distal halves of the lobe oscillate faster than isolated proximal halves.

## INTRODUCTION

Rhythmic patterns of electrical activity are features shared by olfactory organs of a multitude of phylogenetically diverse animals. In mollusca, the local field potential (LFP) of the central olfactory organ of the terrestrial mollusks *Limax maximus* (Gelperin and Tank 1990) and *Helix pomatia* (Schütt and Basar 1994) oscillate continuously. Further, in *Limax* the oscillations take the form of propagating electrical waves, whose spatial phase is modulated by the presence of odors (Delaney et al. 1994). In arthropoda, recent work with locust shows that odor induces spatially coherent oscillations within the mushroom bodies, an organ analogous to the mammalian olfactory cortex (Laurent and Naraghi 1994). Interestingly, a large body of evidence from *Drosophila* implicates the mushroom body as a locus of associative learning in olfactory tasks (Davis 1993). At the level of chordata, oscillatory electrical activity is a salient feature of most teleost, amphibian, reptilian, and mammalian olfactory bulbs and the olfactory cortex of mammals (Adrian 1942; Beurman 1975; Döving 1966; Gerard and Young 1937). In the olfactory bulb these take the form of fast, spatially coherent oscillations that are induced by odor (Adrian 1942; Freeman 1975; Gerard and Young 1937). Oscillations in the mammalian olfactory bulb subsequently drive oscillatory waves of electrical activity across the piriform cortex (Ketchum and Haberly 1991).

Here we investigate the spatiotemporal dynamics of oscillatory activity in *Limax*. In addition to exhibiting oscillations, the olfactory system in *Limax* has additional attributes that support its choice as a model olfactory processing network. First, olfaction is the only sense available to *Limax* for perception at a distance. An acute olfactory sense enables *Limax* to forage (Kittel 1956) and home (Gelperin 1974) over distances of meters in response to fluctuations in airborne odors. Odor cues can also be used

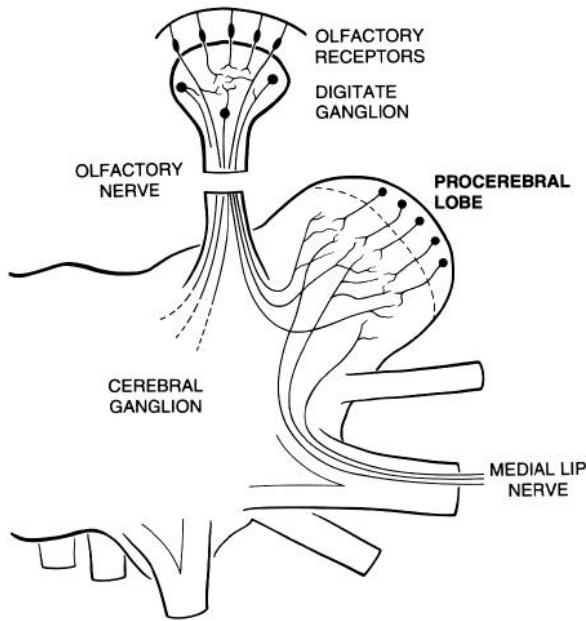


FIG. 1. Schematic diagram of the cerebral ganglion and superior tentacle of *Limax maximus*. The procerebral (PC) lobe receives input from the superior nose, consisting of olfactory neuroepithelium and digitate ganglion, via the olfactory nerve as well as input from the inferior nose via the medial lip nerve.

to condition the behavior of *Limax* with a breadth and effectiveness that rivals the results associated with vertebrate species (Sahley et al. 1992; Yamada et al. 1992). Second, anatomic and functional studies suggest that the central olfactory organ, the procerebral (PC) lobe, performs essential processing that regulates motor behaviors that are triggered by olfactory stimulation (Fig. 1). The PC lobe contains a relatively large number of neurons,  $\sim 10^5$ , that form extensive interconnections within both cell-rich and process-rich regions; the latter is a confluence of extrinsic input and output fibers (Chase and Tollozcko 1993). Additional anatomic studies show that the lobe is the dominant recipient of afferent input from both inferior and superior noses (Gelperin et al. 1993). Last, there is an observed link between odor-mediated activity in the lobe and activation of motor outputs (R. Gervais, K. R. Delaney, D. Kleinfeld, and A. Gelperin, unpublished observations; see also Chase and Tollozcko 1989).

We focus on the dynamics of electrical activity in the PC lobe of *Limax* and ask the following questions. 1) What are the electrophysiological properties of neurons in the lobe? 2) What are the spatiotemporal patterns of electrical activity throughout the lobe? 3) What is the relation between these patterns and the electrophysiology of the underlying neurons? 4) What is the effect of perturbations on the patterns of activity? To answer these questions we make extensive use of optical imaging techniques in conjunction with dyes whose spectral properties are sensitive to membrane potential (Grinvald et al. 1988; Salzberg et al. 1973). Previous studies by Cohen, Kauer, and others (Cattarelli and Cohen 1989; Cinelli and Salzberg 1990, 1992; Kauer 1988; Kauer et al. 1987; Orbach and Cohen 1983; articles in Schild 1990) suggest the utility of these techniques to study patterns of electrical activity in the intact olfactory system.

Aspects of the work presented here have appeared in abstract form (Fee et al. 1992; Gelperin et al. 1992) and in a brief report (Delaney et al. 1994). Here we expand on the range of issues covered in the brief report and expound in detail on all aspects of our work. Particular emphasis is placed on exploring the large-scale dynamical behavior of electrical activity in the isolated lobe and in lobes subject to a spectrum of chemical and physical perturbations. Further, we show how the large-scale electrical activity of the lobe, observed optically, can be decomposed in terms of the observed electrophysiology of the underlying neurons. The effect of natural odor stimuli on the dynamics and the relation of activity in the lobe to motor outputs will be presented in a forthcoming work.

## METHODS

### Preparation

PC lobes are removed from 1- to 5-g animals that are hatched and raised in a controlled environment (Wieland and Gelperin 1983). The animals are anesthetized by immersion in ice for 10 min, after which the brain and buccal mass are quickly removed and transferred to chilled ( $3-5^{\circ}\text{C}$ ) isotonic saline composed of the following (in mM): 52 NaCl, 4.2 KCl, 7  $\text{CaCl}_2$ , 4.6  $\text{MgCl}_2$ , 0.4  $\text{NaH}_2\text{PO}_4$ , 5  $\text{NaHCO}_3$ , 10 glucose, and 5 *N*-2-hydroxyethylpiperazine-*N*-2-ethanesulfonic acid (HEPES) buffer, pH 7.6]. The PC

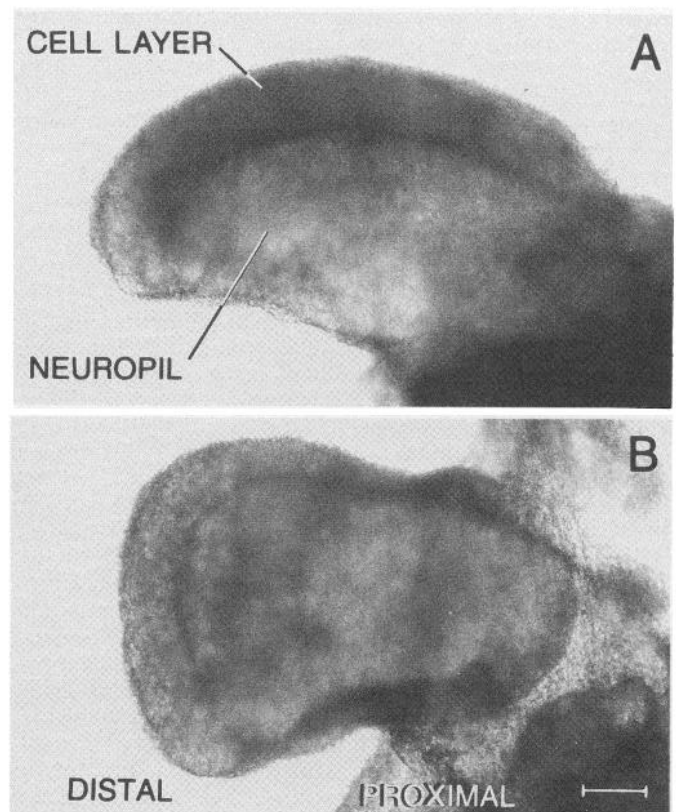


FIG. 2. Photomicrographs of the desheathed isolated PC lobe. *A*: lateral view. A relatively dense layer of somata, 6–8  $\mu\text{m}$  diam, extends across the apex to comprise the posterior face (top edge in this view) of the lobe. The anterior surface (bottom edge in this view) is comprised mainly of neuropil. *B*: posterior view. The major fraction of the cell layer is visible. Scale bar is 100  $\mu\text{m}$ .

lobes appear as symmetrical protuberances from the cerebral ganglion (Chase and Tolloczko 1993). They are severed from the cerebral ganglia near their attachment site, desheathed and pinned via nerves to a silicone elastomer-coated (Sylgard; No. 184; Dow Corning) dish for recording. For some optical measurements, lobes are embedded in 4% (wt/vol) low-melting point agarose (No. A-5030; Sigma, St. Louis, MO) to reduce motion (Mooney and Waziri 1982).

The cell layer of the PC lobe is most clearly discerned from the layer of neuropil when the isolated lobe is positioned on its side (Fig. 2A). Note how the cell layer surrounds the posterior face of the lobe and rolls around the tip that lies distal to the cerebral ganglion. The major part of the cell layer, except for those neurons that lie below the distal edge, is visible with the lobe positioned with the posterior face up (Fig. 2B). This orientation allows changes across the face of the cell layer to be imaged and offers greater mechanical stability.

Fractions of lobes are prepared by surgically transecting a pinned lobe, isolated from the cerebral ganglion, with sharp microelectrodes. For these preparations, the saline is augmented with 1 mg/ml bovine serum albumin. The fragments are isolated in separate dishes and held in place by a cage of microdissection pins.

### Electrical measurements

LFPs are obtained with large-bore (3- to 5- $\mu\text{m}$  tip) glass electrodes,  $R \leq 1 \text{ M}\Omega$ , filled with isotonic saline. Signals are recorded with a patch-clamp amplifier (model EPC-7; List, Eberstadt, Germany) operated in the voltage-clamp search mode and subsequently low-pass filtered at 30 Hz (model 113; Princeton Applied Research, NJ). Perforated patch recordings (Horn and Marty 1988) are obtained with polished glass electrodes,  $R \sim 15 \text{ M}\Omega$ , filled with 50 mM KCl, 3 mM  $\text{MgCl}_2$ , 10 mM HEPES buffer, and 0.1% (wt/vol) nystatin, pH 8.0 and connected to a patch-clamp amplifier (model EPC-7; List, Eberstadt, Germany) operated in the current-clamp mode; the antifungal antibiotic nystatin increases permeability of the membrane to monovalent cations. Whole cell patch recordings are obtained similarly, but without the use of nystatin.

### Staining and optical measurements

We record voltage-dependent changes in the fluorescent yield of preparations stained with 1-(3-sulfonatopropyl)-4- $\beta$ -2-(di-*n*-butylamino)-6-naphthyl]vinyl]pyridinium betaine (di-4-ANEPPS; No. D1199; Molecular Probes, Eugene, OR) (Loew et al. 1992). The dye is prepared as  $\sim 1\%$  (wt/vol) stock solution in 70% (v/v) ethanol/water and diluted to  $\sim 0.002\%$  (wt/vol) in isotonic saline just before use. This dilution scheme appears critical for good dispersion of the dye without the use of detergents. The preparation is stained at room temperature for at least 1 h in excess volume of the dye solution.

The distribution of dye throughout the lobe is assayed by examining thin sections of stained preparations. Lobes are immersed in a 1-ml aliquot of fresh egg white, rapidly frozen in isopentane chilled in dry ice, transferred to a Bright cryostat (Hacker, Fairfield, NJ), sectioned at 6  $\mu\text{m}$  along the distal-proximal axis, thaw-mounted onto No. 1 glass coverslips, and visualized with oil-immersion optics focused through the glass. We observe that the neuropil and cell layer are well stained (Fig. 3A). Particularly heavy staining is present in fine processes that appear to closely follow the contours of faintly stained profiles (arrow in Fig. 3B). These palely stained profiles could be identified as neurons on the basis of their size after counterstaining with cresyl violet (Fig. 3C), an indicator of cytoplasmic and nuclear material. Thus the voltage-sensitive dye appears to predominantly stain fine processes between neurons in the cell layer.

The optical system (Fig. 4) is based on an upright microscope (UEM; Zeiss, Thornwood, NY) modified for imaging at low magnification. Epillumination is accomplished with a  $546 \pm 5\text{-nm}$  (center  $\pm$  HWHM) band-pass excitation filter (No. 546DF10; Omega, Brattleboro, VT), a 580-nm dichroic mirror (No. 580 DRLP; Omega), and a 590-nm long-pass emission filter (No. OG590; Schott, Duryea, PA). The source is a 100-W quartz tungsten lamp (Xenophot HLX; Osram, Berlin). The objective is either a  $f = 4 \text{ mm}$ , 0.75 NA,  $\times 40$  water immersion lens (No. 46-17-02; Zeiss) or a  $f = 5.1 \text{ mm}$ , 0.5 NA,  $\times 40$  extra-long-working-distance lens (No. 78776; Nikon, Garden City, NY). The power at the preparation is typically 5  $\mu\text{W}$ . The emitted light is detected with either an array of seven photodiodes or a cooled charge coupled device (CCD).

The array of photodiodes is constructed from EG&G model UV 100 photodiodes (Montgomeryville, PA) arranged as a hexagonal lattice and situated at the back focal plane of the objective (Fig. 4). The output current of each diode is linearly proportional to the intensity of emitted light in its field of view,  $\sim 1.5\%$  of the total field or a 40- $\mu\text{m}$ -diam spot. The output current is fed to an operational amplifier (No. OPA111; Burr-Brown, Tucson, AZ) configured as a current-to-voltage converter with a  $10^9 \Omega$  feedback resistance and situated immediately behind the diode. The resultant voltage is high-pass filtered at 0.03 Hz (1-pole RC filter with electronic reset), further amplified and low-pass filtered at 35 Hz (5-pole Butterworth filter; No. LTC1062; Linear Technology, Milpitas, CA). The limiting source of noise is photon statistics (shot noise).

The average transmembrane voltage change in the field of each detector is linearly proportional to the fractional change in emitted light, i.e.

$$\Delta V(t) \equiv -\alpha \frac{\Delta F(t)}{F} = -\alpha \frac{F(t) - F}{F} \quad (1)$$

where  $\alpha$  is a constant of proportionality,  $F(t)$  is the intensity of emitted light measured at time  $t$  and

$$F = \frac{1}{T} \int_0^T dt F(t) \quad (2)$$

is the time-averaged output. The constant  $\alpha$  is, in general, species and preparation specific (Delaney et al. 1992; Ross and Reichardt 1979); here  $\alpha \approx 10^4 \text{ mV}$ . Given the small size of the average transmembrane potential in the lobe (RESULTS) relative to  $\alpha$ ,  $\Delta F(t)$  is well approximated by the high-pass filtered detector output, and  $F$  is well approximated by the unfiltered detector output. The optical signal we report is the ratio  $-\Delta F/F \equiv -\Delta F(t)/F$ .

The CCD camera (model CH220 with Thomson 7883 detector, 500 kHz 12-bit analog-to-digital converter and NuBus interface; Photometrics, Tucson, AZ) operates in frame-transfer mode (Lasser-Ross et al. 1991) under the control of a Macintosh IIfx computer (Apple Computer, Cupertino, CA). The image present at the back focal plane of the objective is demagnified and focused onto a  $\sim 2 \text{ mm}$  by  $2 \text{ mm}$  region of the CCD with a projection and zoom lens assembly (Fig. 4) constructed from optical bench components (Microbank series; Spindler-Hoyer, Milford, MA). Consecutive images of the entire field, with a typical resolution of 6  $\mu\text{m}$  per pixel for a  $90 \times 90$ -pixel image, are acquired at frame rates up to 16 Hz. Subregions of the field can be acquired at proportionately higher rates.

Images are analyzed with the Interactive Display Language (Research Systems, Boulder, CO) graphics package run on a Sparcstation 2 (Sun Microsystems, Mountain View, CA). The intensity of emitted light at time  $t$  for a CCD element centered at  $(x, y)$ , where  $x$ ,  $y$ , and  $t$  are discrete variables, is denoted  $F(x, y, t)$ . The optical signal derived from  $F(x, y, t)$  is presented in one of three ways (Fig. 5). 1) The first way is two-dimensional spatial maps (Fig. 5A).

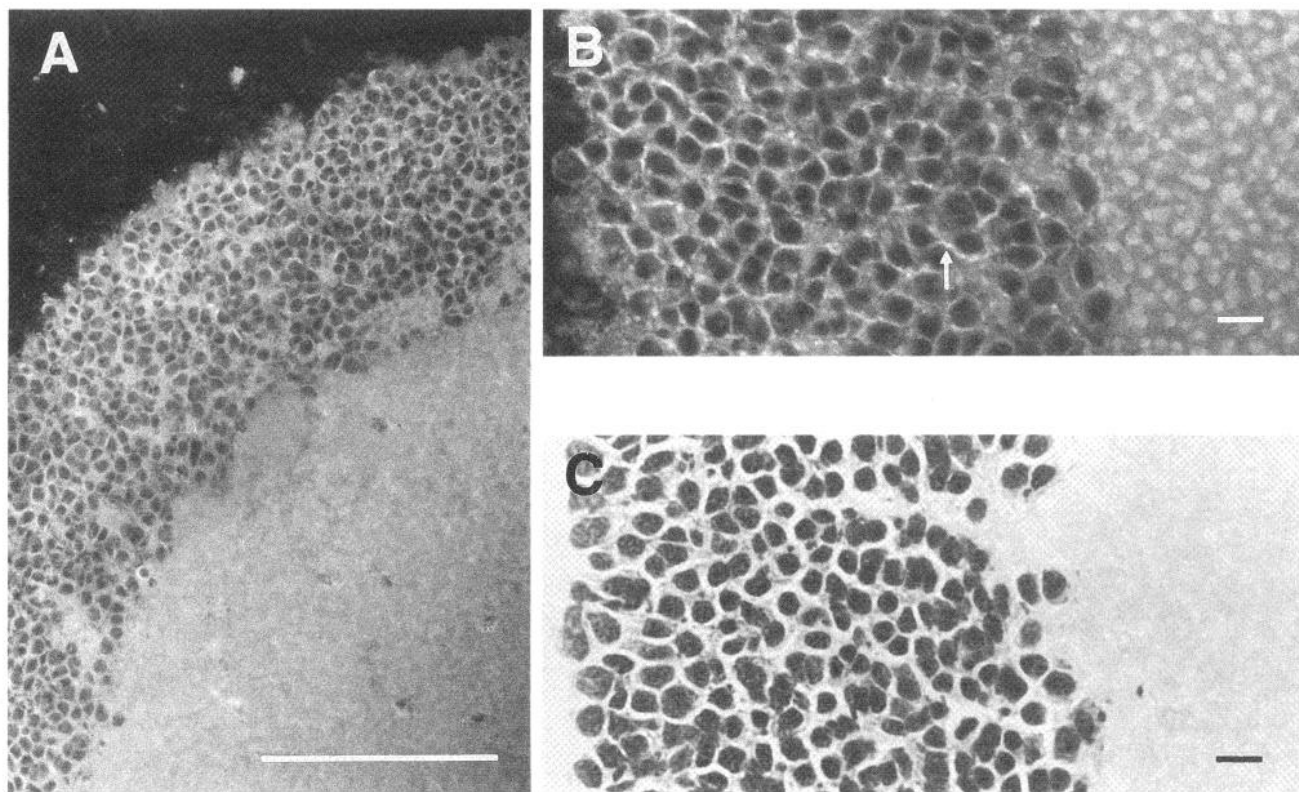


FIG. 3. Photomicrographs of a stained preparation. *A*: fluorescent image of a stained section. Note the clear delineation between the cell layer and neuropil and the uniform staining of the neuropil. Scale bar is 100  $\mu\text{m}$ . *B*: higher magnification fluorescent image of a stained section. Note the staining of membrane and interstitial regions only in the cell layer. Scale bar is 10  $\mu\text{m}$ . *C*: mixed bright-field and Normarski image of a companion section to that shown in *B* that is stained with cresyl violet to highlight cytoplasmic material. Note the dark somata and light, unstained processes. Scale bar is 10  $\mu\text{m}$ .

Each map is spatially filtered by convoluting the original image with a triangular window, typically 5 pixels on edge. Different levels of change in emission are coded by false-color. We chose a scheme with yellow/red indicating depolarization ( $-\Delta F/F > 0$ ) and blue/violet hyperpolarization ( $-\Delta F/F < 0$ ). The boundaries of each map are determined from the fluorescent image  $F(x, y, t = 0)$ . 2) The second way is space-time maps of activity along  $\hat{x}$  (Fig. 5*B*). The optical signal along a specified length of  $\hat{y}$  is averaged to form a one-dimensional stripe along  $\hat{x}$ . 3) The third way is line plots of the change in optical signal versus time for select regions (Fig. 5*C*). A box is defined that encompasses the desired region, and the average fractional change in fluorescence within the box is calculated.

## RESULTS

### *Electrophysiology of individual neurons*

The characteristics of neurons across the posterior surface of the cell layer are surveyed with intracellular recording techniques. As the neurons are small,  $\sim 6\text{--}8\ \mu\text{m}$  diam, we typically make use of the perforated-patch technique (Horn and Marty 1988). We also record the LFP<sup>1</sup> in the vicinity of the patch electrode as a means to facilitate com-

parisons between cells. Two classes of intracellular responses are observed over a sample of 77 successful perforated-patch recordings.

Neurons in one class, denoted bursting neurons, comprise  $\sim 10\%$  of the sample and produce periodic bursts of action potentials (Fig. 6*A*). The period at room temperature is  $\sim 1.4\ \text{s}$ , as previously observed in the field potential (Gelperin et al. 1993). Several characteristic features are associated with the bursts. 1) Each burst coincides with an event in the LFP. 2) The instantaneous rate of firing within a burst tends to accelerate toward the end of a burst. 3) The bursts are followed by a period of hyperpolarization and subsequently a depolarizing afterpotential (arrow in Fig. 6*A*). It is unclear to what extent the hyperpolarization is derived from synaptic input or represents a hyperpolarizing afterpotential. 4) There is a small but significant chance<sup>2</sup> for spikes to occur concomitant with the depolarizing afterpotential. In the case of a single spike, there is no event in the associated LFP (\* in Fig. 6*B*). However, when two or more spikes occur, as is typical in these double events, there is an associated double event in the LFP (\*\* in Fig. 6*B*).

<sup>1</sup> The LFP is a measure of current flow through the extracellular space. Its shape and polarity depend of the distribution of ionic current flow in the preparation and on the depth of the tip of the electrode. Close to the surface of the cell layer the LFP is primarily positive going, whereas deep in the cell layer it is negative going (Gelperin et al. 1993).

<sup>2</sup> The occurrence of double events varies greatly between preparations. A "typical" preparation produces double events approximately every 20 periods. However, some preparations produce no double events for times on the order of  $10^3$  periods. Maintaining a lobe in a restricted space that is not perfused appears to lead to a high prevalence of double events; this suggests that they are triggered by the release of endogenous modulators.

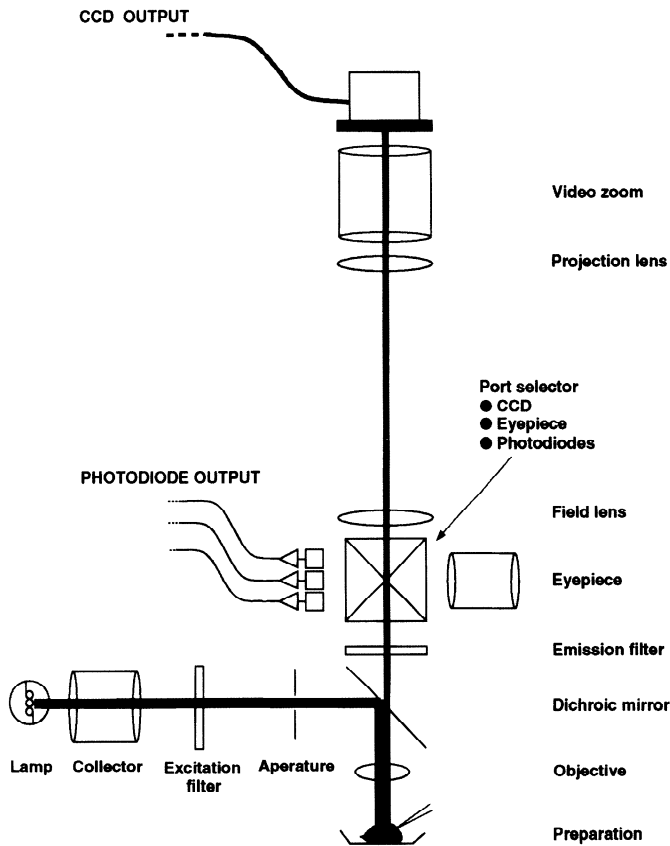


FIG. 4. Schematic of the experimental setup used for simultaneous electrical and optical measurements and for imaging large-scale activity in the lobe. The optical system consists of an epillumination microscope with additional lenses to conveniently control the size of the image projected onto the charge coupled device (CCD) array. In detail, the real image present at the back focal plane of the objective is imaged at infinity by the projection lens ( $f = 160$  mm) and subsequently focused onto the CCD array by the video zoom lens (typically set at  $f = 16$  mm for an overall magnification of  $\times 4$  with a  $f = 4$ -mm objective). The field lens ( $f = 300$  mm) prevents vignetting.

Neurons in the second class, denoted nonbursting neurons, are the major fraction of cells in the lobe and do not produce periodic bursts of action potentials. The characteristic features associated with these cells are as follows. 1) They exhibit strong, periodic inhibitory postsynaptic potentials (IPSPs) during every event in the LFP (Fig. 7A). This includes double events (Fig. 7B). Previous work shows that the IPSP reverses at approximately the expected  $\text{Cl}^-$  reversal potential (Gelperin et al. 1993). 2) The average rate of spiking is low, 0.5 spikes per period. However, a few cells show as many as 6 spikes per period. 3) Double events in the LFP appear as consecutive hyperpolarizations (\*\* in Fig. 7B). The amplitude of the second hyperpolarization is less than that of the first, again consistent with only partial repolarization of the cell.

The relatively low density of bursting neurons in the lobe prevents us from making simultaneous intracellular measurements on both bursting and nonbursting neurons. On the other hand, given that the intracellular measurements are accompanied by measurements of the LFP, we can estimate the relative timing between the intracellular potentials of the two classes of cells. We leave one pair of intracellular

and LFP records unchanged, dilate the time scale of the second pair of records to account for differences in the period of the oscillation, and then align the LFPs from the two separate measurements. This is shown for a bursting and nonbursting neuron situated near the middle of the lobe (Fig. 8). The onset of the hyperpolarization occurs close to the trailing edge of the burst. Collectively, our results suggest, but do not prove, that the hyperpolarization in nonbursting cells is driven by multiple spikes from the bursting neurons.

#### Dual-site electrical measurements

Is there a spatial structure to the oscillatory activity in the lobe, as has been suggested for the oscillations in the mammalian olfactory bulb (Freeman 1978)? To examine this

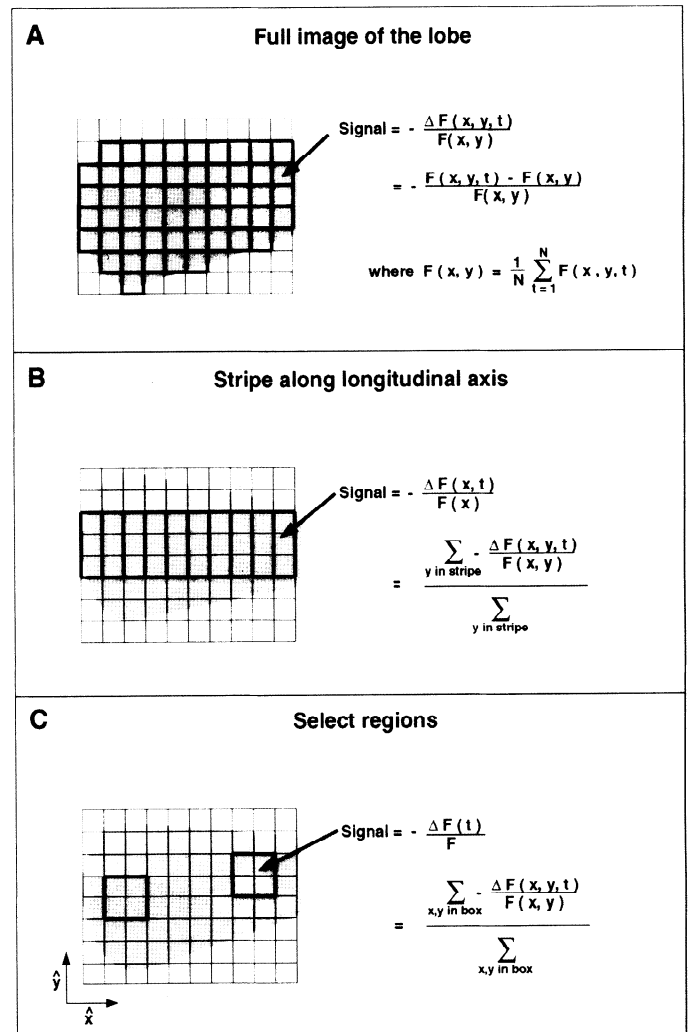


FIG. 5. Schematic of the data analysis procedures used to calculate optical signals from successive 2-dimensional images of emission from stained lobes. The pixel structure of the CCD is caricatured as an  $8 \times 10$  grid. Regions that correspond to the reported optical signal are highlighted by thick lines. A: 2-dimensional spatial map. The change in emission for all pixels that encompass the lobe is reported (e.g., Fig. 14A). B: 1-dimensional spatial map. The optical signal is calculated for a narrow stripe parallel to the long axis ( $\hat{x}$ ) of the lobe (e.g., Fig. 16A). C: no spatial dimensions. The optical signal is calculated for a few spots on the lobe (e.g., Fig. 14B).

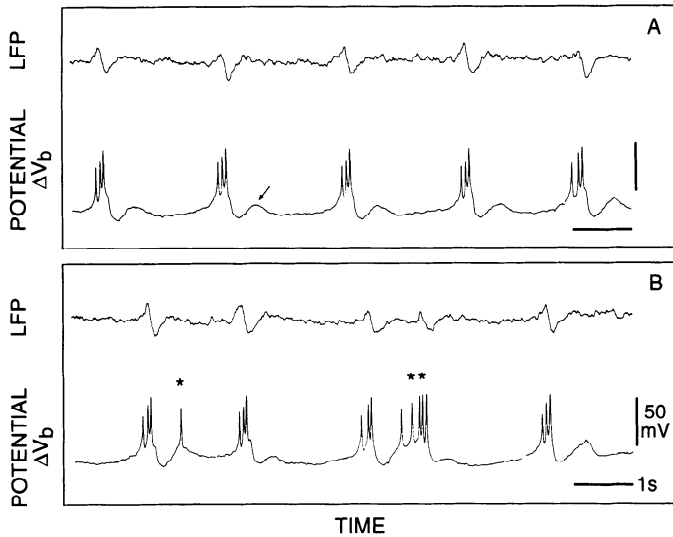


FIG. 6. Intracellular recordings from a bursting neuron along with the simultaneous recorded local potential (record 10.11.90.3). Note that the scaling of the local field potential (LFP) is arbitrary. *A*: typical behavior. Note the regular, periodic bursting and the depolarizing afterpotential (arrow). *B*: behavior during an epoch of extra spikes. The occurrence of a single extra spike (\*) does not lead to an extra event in the LFP, whereas the occurrence of 2 or more spikes does (\*\*).

possibility we perform simultaneous intracellular measurements on cells at nearly opposite ends of the cell layer in a preparation with posterior exposure ( $n = 6$ ). Measurements are made with conventional whole cell patch rather than perforated-patch techniques; the later technique requires that cells be patched within the diffusion time for nystatin to reach the pipette tip (METHODS), and this constraint proved too confining for dual-site measurements. We observe similar waveforms at sites spaced  $\sim 300 \mu\text{m}$  apart with respect to the long axis of preparations (Fig. 9).

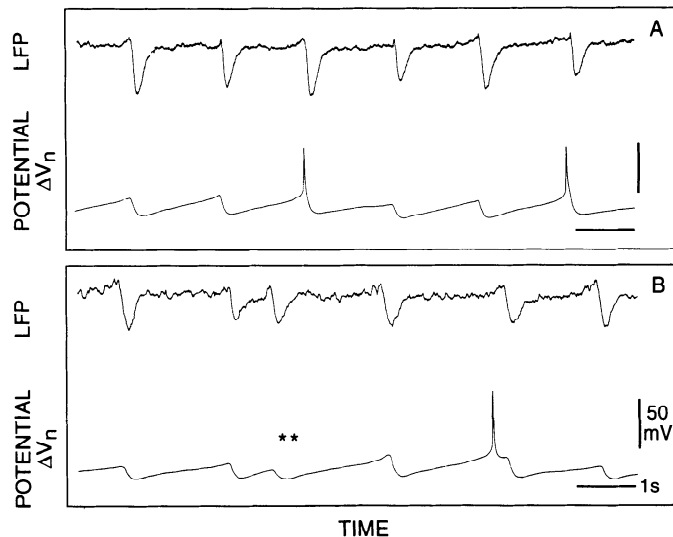


FIG. 7. Intracellular recordings from nonbursting neurons along with the simultaneous recorded local potential. Note that the scaling of the LFP is arbitrary. *A*: typical behavior. Note the regular, periodic inhibitory post synaptic potentials and the low probability of spikes ( $V_{\text{rest}} = -57 \text{ mV}$ ; 6.16.92). *B*: records from a preparation that shows double events. Note that the 2nd of the 2 events (\*\*) has a reduced magnitude ( $V_{\text{rest}} = -58 \text{ mV}$ ; 10.19.90.4).

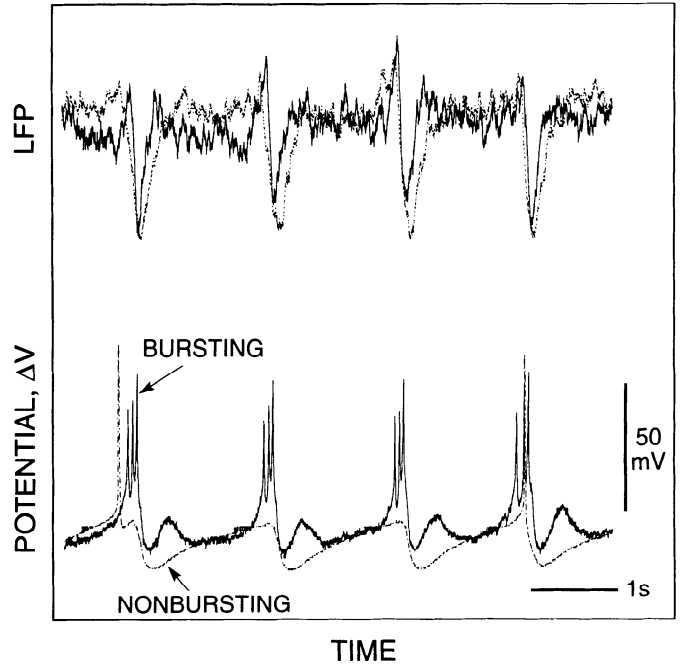


FIG. 8. Relative timing between the output of bursting and nonbursting neurons. A record of a bursting cell (solid line; 10.11.90.3) and one of a nonbursting cell (hatched line; 9.17.92.1), taken from the same location on different preparations, are combined to estimate the relative timing between events in the 2 cell types. The concomitant LFPs are taken from sites close to the intracellular electrode and deep in the cell layer. To overlay the records, we 1st linearly expanded the time base of the record for the nonbursting cell (by 36%) to match the periodicity of the record for the bursting cell. We then aligned the LFPs of the 2 records by their leading edges.

There are, however, clear differences in timing, as seen either in the onset time for the hyperpolarization or in the time-to-peak. This shows that there are steady-state phase differences in electrical activity across the lobe.

We note for completeness that simultaneous measurements of the LFP may give ambiguous results for assaying differences in timing across the lobe. First, the shape of the signal depends on the depth of the electrode (Gelperin and Tank 1990). Second, the LFP reports the average intrinsic and synaptic currents that flow through the extracellular space. The spatial extent of this average may be a significant

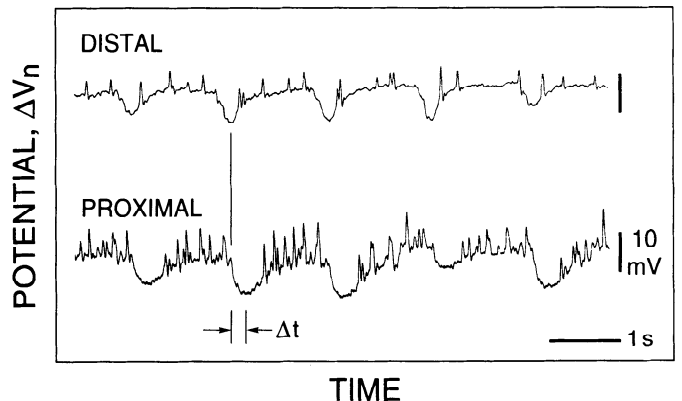


FIG. 9. Simultaneous dual-site whole cell measurement from nonbursting cells in the lobe. The fast events are attenuated spikes that result from leaky seals in these recordings (7.8.92).

fraction of the size of the lobe. This may have precluded the detection of phase differences in previous studies (Gelperin et al. 1993).

#### Optical measurements at select locations

As a means to routinely measure the large-scale electrical activity across the lobe, we evaluate optical methods based on the use of voltage-sensitive dyes that report the cell membrane potential (Grinvald et al. 1988). We consider first measurements from single locations, 50  $\mu\text{m}$  diam, on preparations positioned on their side (Fig. 10*A*). This orientation of the lobe allows us to sample the entire cell layer and the neuropil. We observe periodic output from all locations (Fig. 10, *B–G*), although the detailed shapes of the waveforms recorded from the cell layer vary systematically along the longitudinal axis of the lobe. The optical signal has a sharply rising triangle-wave shape at the distal end (Fig. 10*B*), a sharply falling triangle-wave shape at the extreme proximal end (Fig. 10*F*), and a peaklike character at mid locations (Fig. 10, *D* and *E*). The signals at the distal end show weak but consistent evidence of an early, depolarizing event (asterisk in Fig. 10, *B* and *C*; see also Fig. 17). Signals recorded from regions of essentially pure neuropil have a triangle-wave shape similar to that seen near the distal end (cf. Fig. 10, *B* and *G*) and are smaller in amplitude than those observed from the cell layer. Last, there are no signs of photodynamic damage for illumination times up to at least 90 min.

#### Relation between optical and electrical signals

The above results (Fig. 10) show that optical methods provide a reliable means for measuring local, oscillatory activity in the lobe. To interpret the optical signals in terms of the intracellular potentials of the underlying neurons, we performed simultaneous intracellular and optical measurements. In particular, the intracellular potential in nonbursting neurons is recorded simultaneously with the optical signal in an  $\sim 50\text{-}\mu\text{m}$  field that encompasses the cell. We consider first neurons situated near the distal part of the lobe (Fig. 11*A*). The oscillations in both electrical and optical records show the same waveform, and the signals are perfectly in phase with each other. Close examination of the records reveals that both slow fluctuations and relatively fast events in the intracellular potential are consistently reflected in the optical record (e.g., corresponding arrows in Fig. 11*A*). These similarities imply that the optical signal accurately reports the electrical activity of the nonbursting cells in distal regions of the lobe.

The relation between the intracellular signal and the concomitant optical signal measured from the middle part of the lobe is similar to that seen at the distal end (Fig. 11*A*), with the exception that optical signals recorded from middle regions often show relatively sharper positive peaks (Fig. 11*B*). The timing of these peaks is consistent with the burst of action potentials that precedes the hyperpolarization (Fig. 8).

The relative contribution of the bursting cells to the optical signal from the middle region of the lobe is assessed in two complementary ways. In the first assessment, we com-

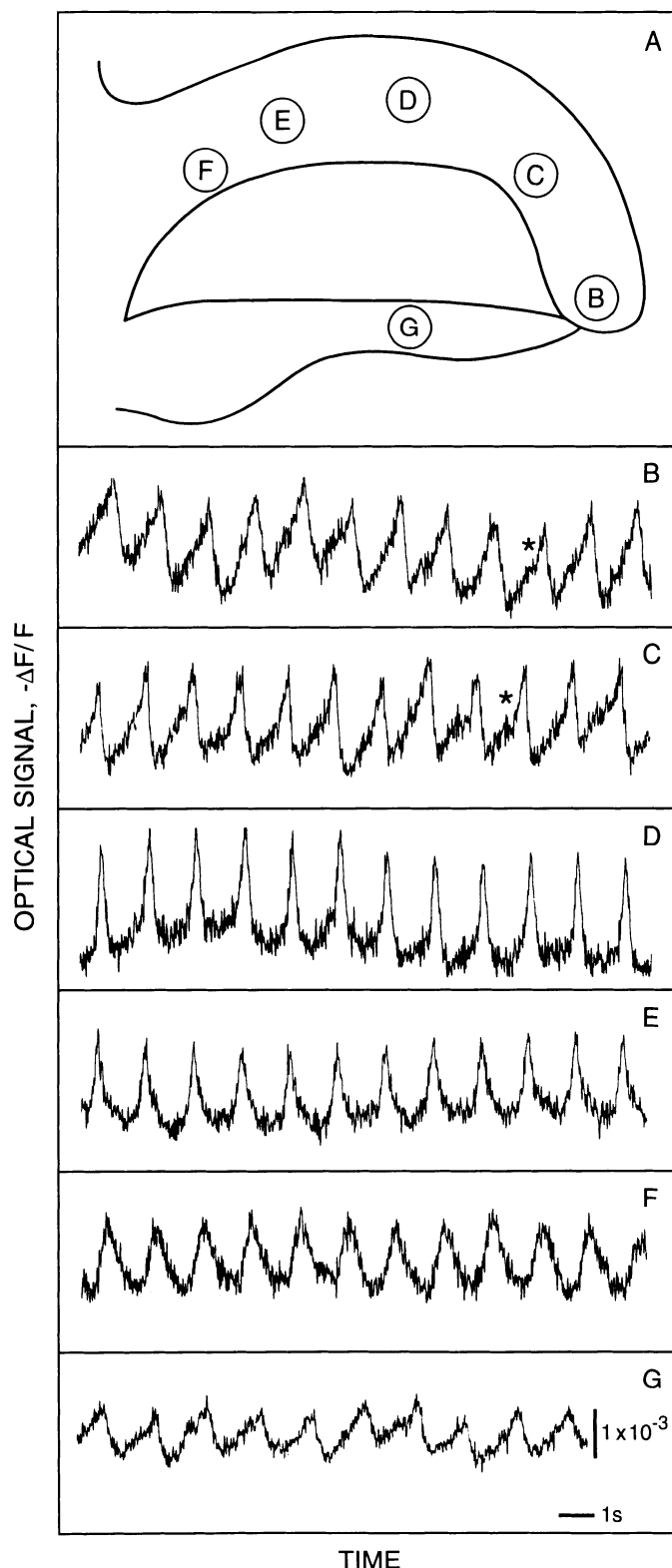


FIG. 10. Optical measurements from different sites on the lobe; lateral exposure. These are not simultaneous recordings. Each measurement corresponds to the signal at a  $\sim 50\text{-}\mu\text{m}$  spot (2.10.92). *A*: cartoon of the lobe, with locations of recording sites. *B–F*: signal from sites in the cell layer, as indicated in *A* (2.5.92.540, .552, .247, .517, .462). The asterisks in *B* and *C* indicate weak, early depolarizing events. *G*: signal from a site with mostly neuropil (2.5.92.651). Note that the scale is the same in all panels.

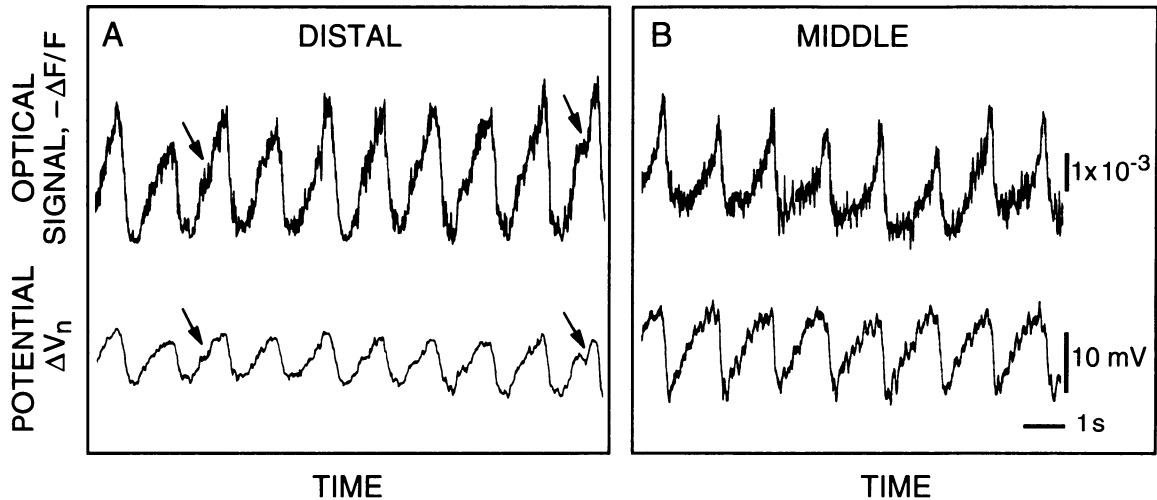


FIG. 11. Simultaneous optical and whole cell patch measurements; lateral exposure. In these measurements, both signals were filtered with identical 5-pole Butterworth low-pass filters (METHODS). *A*: record from a location at the extreme distal end of the lobe (6.11.92.2). The 2 pairs of arrows highlight fast events that are present in both electrical and optical records. *B*: record from a location at the middle of the lobe (6.14.92.2).

pare the optical signal with the simultaneously recorded LFP during double events (\* in Fig. 12). We observe the typical broad optical signal concomitant with single events in the LFP (cf. Figs. 11*C* and 12) but only a positive peak after each of the two events is essentially identical. We recall two features of the intracellular records toward interpreting these data. First, the magnitude of the hyperpolarization in nonbursting cells is reduced on the second event compared with that of the first (Fig. 6*B*) because of the slow recovery of the IPSP. Second, the amplitude and number of action potentials in bursting cells is similar during both the first and second bursts (Fig. 5*B*). Thus the change in the optical signal during the second of the two events (\* in Fig. 12) is likely to reflect the change in behavior of the nonbursting cells.

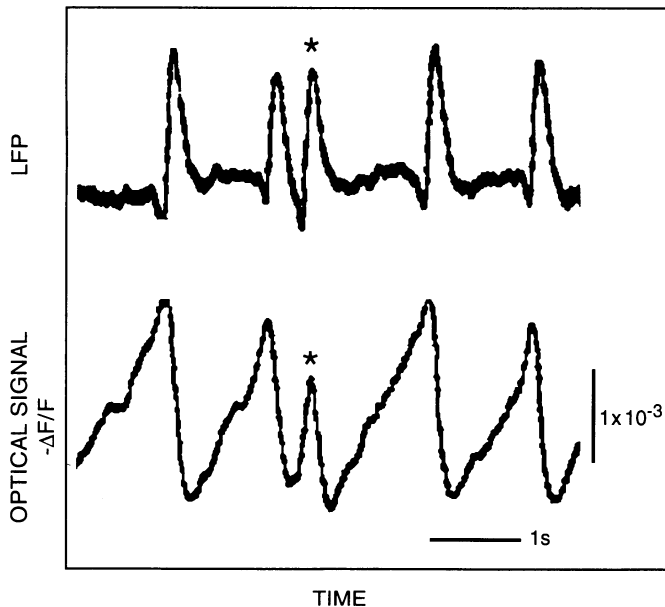


FIG. 12. Simultaneous optical and LFP measurements from a mid-distal location in the lobe during a double event (\*; 10.23.91.8).

In our second assessment we compare the optical signal with the simultaneously recorded LFP during a period in which electrical activity in the nonbursting cells is transiently quenched ( $n = 3$ ). A weak shock to the neuropil results in a local depolarization that induces widespread hyperpolarization throughout the lobe (imaging data not shown). Before the shock, the optical record shows the normal train of IPSPs, and the LFP indicates the concomitant inhibitory currents (Fig. 13). After application of the shock, we observe a deep, prolonged hyperpolarization in both records. The subsequent repolarization is accompanied only by fast, sharp depolarizing events in the optical record and fast inward currents (negative going peaks) in the LFP (\* in Fig. 13). We interpret these fast events as rapid, synchronous firing by the bursting cells. The normal waveform begins to reappear in both the optical and electrical records  $\sim 5$  s after the shock, although the fast events are maintained for up to 30 s.

We conclude that the peak of the optical signal coincides with the burst of action potentials in bursting cells (probably the trailing edge of the burst, Fig. 8) and with the onset of the inhibitory input to the nonbursting cells. The triangle-like component of the optical waveform reflects the time course of the IPSPs in nonbursting cells, whereas the peaked component reflects the burst of action potentials in bursting cells. These results imply that any difference in the timing of optical signals observed in images of the lobe will correspond to differences in subthreshold and suprathreshold activity of the underlying neurons. Further, the above data suggest that bursting cells make a relatively larger contribution to the optical signal at locations near the middle of the lobe versus those at the distal end; we return to this issue in the context of time-resolved images of activity across the lobe (Fig. 16).

#### Imaging of large-scale activity

Spatiotemporal maps of electrical activity are inferred from optical images of the change in emission (Fig. 5*A*). We observe a wave of depolarization, followed by hyperpo-

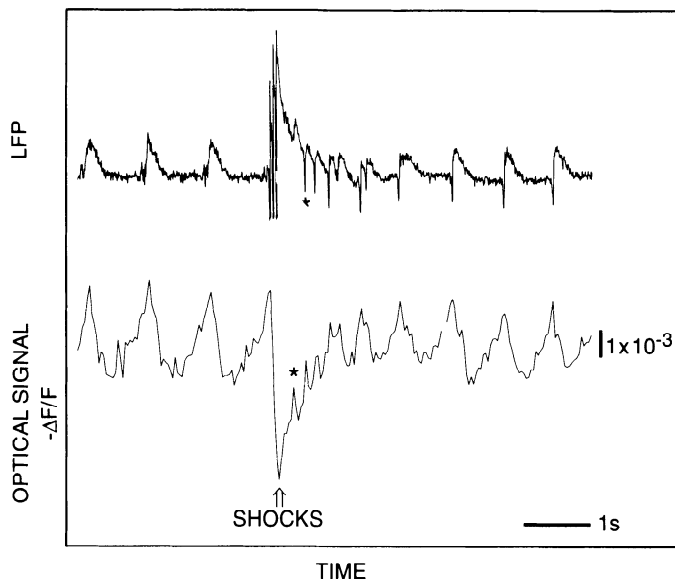


FIG. 13. Simultaneous optical and LFP measurements from the middle of the lobe. Three weak shocks ( $100 \mu\text{A}$  delivered for 1 ms at 20-ms intervals) are delivered to a central region in the neuropil. Note the fast events that occur during the repolarization after the shock (\*; 7.25.23s, 7.25.92.1052).

larization, that travels along the axis of the preparation from the distal end toward the cerebral ganglion (Figs. 14 and 15). The direction of the wave is consistent with the timing differences observed in the dual-site intracellular measurements (Fig. 9). Viewed laterally (Fig. 14A), depolarization begins near the distal end of the lobe among cell somata and, concomitantly, relatively weak depolarization begins more proximally within an anterior region of neuropil (cf. black and red plots in Fig. 14C). The stronger depolarization traverses the length of the cell layer, as shown by the red region in Fig. 14A, until it ebbs (cf. black and red plots in Fig. 14B). The propagation of depolarization is followed by a similar propagation of hyperpolarization. Finally, the cycle begins anew.

When the entire cell layer is observed in a posterior exposure, depolarization and subsequent hyperpolarization are seen to begin at the distal tip (Fig. 15, A and C). They move as a continuous band across the surface of the lobe.<sup>3</sup> Under optimal conditions, activity is seen to propagate past the cell layer and slightly into the cerebral ganglion before it ebbs (Fig. 15A). The shape of the waveform is essentially uniform within a band (cf. black and red bands in Fig. 15B), but varied along the direction of propagation (cf. black and red bands in Fig. 15C) similarly to that seen with the lateral exposure (Fig. 14). Note that a posterior exposure of the preparation offers mechanical stability that is crucial for experiments with odor stimuli, but that the full extent of the timing difference between distal and proximal ends is often difficult to discern because of the substantial overlap of cells at the distal end (Fig. 2A). Thus we typically

<sup>3</sup> Waves along the transverse as well as longitudinal axes of the lobe are noted in a preliminary report (Fee et al. 1992). The transverse waves in this early report are now believed to be the result of nicks to the preparation, as discussed in a later section.

record only part of the phase difference between distal and proximal ends of the lobe.

We previously argued that the optical signal contains contributions from bursting and nonbursting neurons. We now consider the decomposition of spatiotemporal images of the electrical activity in the lobe into the separate contributions from the two cell classes. On the one hand, this analysis serves to quantify our previous arguments regarding the interpretation of the optical signal in terms of the underlying intracellular events. On the other hand, it provides a map of the spatial distribution of the two cell classes along the length of the lobe, along with a map of as yet uncharacterized intracellular signals.

Electrical activity is imaged along a relatively narrow stripe ( $\sim 100 \mu\text{m}$ ) along the middle of the face of the lobe (Fig. 5B). We achieve a relatively high frame rate with this reduced image (27 Hz; METHODS) and, by averaging pixels along the transverse direction, a relatively high signal-to-noise ratio. The resulting space-time map is shown in Fig. 16A, and the average over six periods is shown in Fig. 16E. Because the electrical activity appears uniform along the transverse axis of the unperturbed lobe (Fig. 15B), these one-dimensional images in the longitudinal axis capture the complete spatial variation of activity. In the central region of the stripe, we observe a band of depolarization (red) immediately followed by successive bands of hyperpolarization (blue). This sequence is consistent with our previous analysis of the relation between the optical and intracellular signals. The instantaneous slope of these bands corresponds to the speed of the wave ( $\sim 1 \text{ mm/s}$  for the present data). The break in the band of hyperpolarization (green area in box of Fig. 16E) corresponds to the depolarizing afterpotential of bursting cells (arrow in Fig. 6A) that adds to the hyperpolarization of the nonbursting cells. At distal locations in the stripe we clearly observe a relatively early depolarizing event (\* in Fig. 16E), as suggested by spot measurements (Fig. 10, B and C). At the proximal end the depolarization ebbs, although there is still periodic hyperpolarization. The form of the signals at either end of the lobe is different from that suggested by our previous analysis of the relation between the optical and intracellular signals.

We now consider quantitatively the relation between the optical signal along the longitudinal axis and the observed intracellular signals. Our analysis makes use of two assumptions. First, we recall that fine processes make the dominant contribution to the optical signal (Fig. 3). We assume that the neurons are nearly equipotential, so that intracellular potentials recorded at the soma reflect the potential throughout their processes. Second, we assume that the relative phase between the bursting and nonbursting cells at each location along the lobe is fixed<sup>4</sup>, whereas, in fact, we have only established the phase relation at the middle of the

<sup>4</sup> More generally, the bursting cells and the nonbursting cells may be allowed to have independent phase delays in our analysis, i.e.  $-\Delta F(x,t)/F(x) \approx A_b(x)\Delta V_b[t + \tau_b(x)] + A_n(x)\Delta V_n[t + \tau_n(x)]$ , where  $\tau_b(x)$  and  $\tau_n(x)$  are the phase delays for bursting and nonbursting cells, respectively. In practice, the fit of this function to the data appeared good but is numerically unstable in spatial regions where the fit with a single phase delay had a relatively large residual.

lobe (Fig. 8). Given these assumptions, the fractional change in emission at each location in the stripe,  $\Delta F(x,t)/F(x)$  (Fig. 5B), is expressed in terms of contributions from bursting and nonbursting cells,  $\Delta V_b(t)$  and  $\Delta V_n(t)$ , respectively. We seek to approximate the relation

$$-\frac{\Delta F(x,t)}{F(x)} \simeq A_b(x)\Delta V_b[t + \tau(x)] + A_n(x)\Delta V_n[t + \tau(x)] \quad (3)$$

for each value of  $x$ , where  $\tau(x)$  is the phase delay along the longitudinal axis and  $A_b(x)$  and  $A_n(x)$  are the amplitudes of the contribution from bursting and nonbursting cells, respectively. Equation 3 cannot be satisfied at each value of space and time. A best approximation for the three unknown functions is found by minimizing the square of the difference between the two sides of Eq. 3 over all values of time  $t$  (APPENDIX). The results of our analysis are shown in Fig. 16, B–D, F, and G.

We observe that the phase delay  $\tau(x)$  is essentially linear along the length of the lobe (Fig. 16B). Thus, insofar as Eq. 3 is a valid approximation, the onset of bursting and subsequent hyperpolarization varies linearly with distance along the lobe. The absolute contribution from bursting cells<sup>5</sup> to the optical signal reaches a maximum at the central region of the lobe and is barely significant at the distal end (red line in Fig. 16C). On the other hand, the contribution of the nonbursting cells plateaus at its maximum value along the distal region and decreases roughly linearly between the middle and proximal end (black line in Fig. 16C). The relatively large contribution of bursting versus nonbursting cells at the distal end is consistent with the simultaneous electrical and optical measurements (Fig. 11A). The presence of bursting and nonbursting signals at the middle of the lobe is consistent with the waveforms recorded at selected spots (Figs. 10, C and D, and 11B).

The present analysis shows that, in the central region of the lobe,  $\sim 80\%$  of the optical waveform is accounted for in terms of bursting and nonbursting cells with a fixed, relative phase relation. Toward the distal end the fit is less good, and the present analysis provides clear evidence for an early depolarizing event (see also Fig. 10, B and C). Whether this represents a population of bursting cells that fire relatively early compared with the onset of the IPSP in the nonbursting cells, or a new class of neurons is unknown. Last, the fit at the extreme proximal end of the lobe is poor. This reflects in part the lack of a rapid depolarizing event (see also Fig. 10F) and in part the decreased signal amplitude and signal-to-noise ratio.

### Behavior of modified preparations

The direction of propagation of the wave in the isolated, unperturbed lobe is distal to proximal (Figs. 9 and 14–16). We consider two extreme possibilities for the origin of the directionality. 1) It is imposed by dynamics, e.g., a spatial gradient of excitability in a network with diffusive connec-

tions. 2) It is imposed by a neuronal architecture with unidirectional synaptic connections that run distal to proximal.

To distinguish between these two possibilities, we first consider the detection of a gradient of excitability along the longitudinal axis of the lobe. In principle, such a gradient will be manifest as a monotonic increase in the period of oscillation of isolated sections of the lobe cut normal to the longitudinal axis, with the shortest period occurring at the distal end. This assay, of course, assumes that surgically isolated fragments of the lobe will oscillate. We tested this possibility in lobes successively reduced to 0.5, 0.2, and 0.1 of their original size (METHODS). We observe that the largest fragments, 0.5 lobe, made from either distal or proximal portions of the lobe ( $n = 6$ ) always oscillate, as measured optically (Fig. 17A) or via the LFP. Subsequent fragments of 0.2 and 0.1 lobe ( $n = 3$ ) that are taken from the middle to proximal region of the lobe also oscillate, but similarly sized sections from the extreme distal end switch between oscillatory and nonoscillatory behavior (Fig. 17B).<sup>6</sup> Last, the early depolarizing event seen at the distal end of intact lobes (asterisk in Figs. 10, B and C, and 16E) is present in both fragments (\* in Fig. 17, A and B).

We observe that the period of oscillation for isolated distal 0.5 lobes is significantly shorter than for isolated proximal 0.5 lobes, i.e.

$$\frac{T_{\text{distal}}}{T_{\text{proximal}}} = 0.8 \pm 0.1$$

where the mean and standard deviation of the mean are calculated from the ratios of measurements on six preparations. This result strongly suggests that there is a gradient of excitability in the lobe, although not necessarily a linear gradient, with distal regions more excitable than proximal regions.

To determine whether the underlying connectivity is, at least in part, multidirectional, we consider experiments designed to modify the direction of the wave. The first set of experiments involves the use of surgical techniques to make a small cut in a lobe that prevents the normal propagation of activity. A particularly clean example of a change in propagation is seen in a posterior view of a preparation with a small cut along the lateral edge (Fig. 18). Depolarization begins at the edge near the cut and propagates laterally across the preparation (Fig. 18A, frames 6–8, and Fig. 18B). Only then does the depolarization course along the distal to proximal axis (Fig. 18C), as in normal preparations.

As a means to reverse the direction of wave propagation, we consider chemically induced changes in excitability of the lobe. Our goal is solely to address an issue of principle

<sup>6</sup> This result shows that the distal end of the lobe, which apparently contains relatively few bursting cells (Fig. 16B), can produce oscillations. The oscillations are likely to be the manifestation of the early but weak periodic depolarization at the distal end. Note that the rapid switching between a state that oscillates near the normal frequency of the lobe and one without oscillations suggests that local dynamics at the distal end are the result of a Hopf bifurcation, in which periodic motion with small amplitude and high frequency forms about a destabilized state as a control parameter is varied beyond a critical value, as opposed to a saddle node bifurcation, in which periodic motion with large amplitude and low frequency forms (Guckenheimer and Holmes 1983).

<sup>5</sup> The optical signal is proportional to the membrane area of the active neurons within the volume that contributes to a particular detector. Thus the maximum contribution from the bursting and nonbursting cells may be approximately equal even if there is a large disparity in the relative number of somata from the two cell classes.

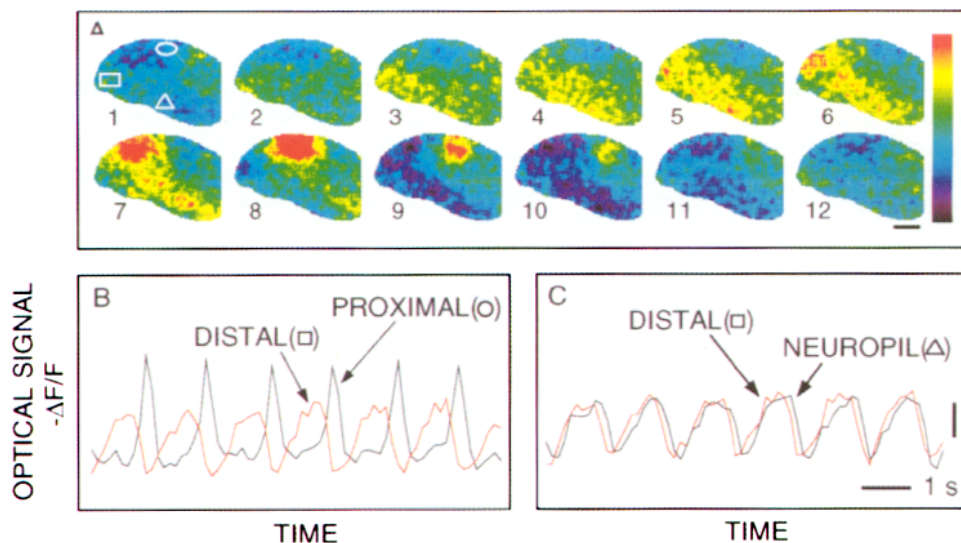


FIG. 14. Propagation of electrical waves along the lobe; lateral view (7.11.92.2s). *A*: CCD sequence of images of activity during a single period. Parameters: 120 ms/frame,  $-\Delta F/F$  (max/min) =  $\pm 0.0025$ , scale bar = 100  $\mu\text{m}$ . *B*: optical signal  $-\Delta F/F$  vs. time for a site at the distal tip (red) vs. one at a proximal location (black; see boxes in panel 1 of *A*). *C*: optical signal  $-\Delta F/F$  vs. time for a site at the distal tip (red) vs. one at a proximal location (black; see boxes in panel 1 of *A*). Scale bar is  $-\Delta F/F = 0.001$ .

about the dynamics in the lobe, and, as such, we evaluate the effect of modulatory agents<sup>7</sup> and changes in the concentration of ionic species on the wave motion without regard to the detailed pharmacological basis of the induced

<sup>7</sup> In addition to the effect of known modulators (Gelperin et al. 1993; Rhines 1989) on the period of oscillations, we found that micromolar concentrations of acetylcholine or carbamylcholine substantially decrease the period of oscillations.

changes. The strongest indication for a reversal of the direction of the wave is observed with reduced ionic concentrations of chloride; 24.2 mM versus 79.4 mM  $\text{Cl}^-$  in standard saline, with gluconate replacing Cl. It is likely that  $\text{Cl}^-$  is the permeant ion for the IPSPs seen in nonbursting cells (Gelperin et al. 1993) and that our manipulation should raise the reversal potential for  $\text{Cl}^-$  by 30 mV. Note that replacement of Cl by gluconate may affect intrinsic cellular properties through a change in osmotic balance.

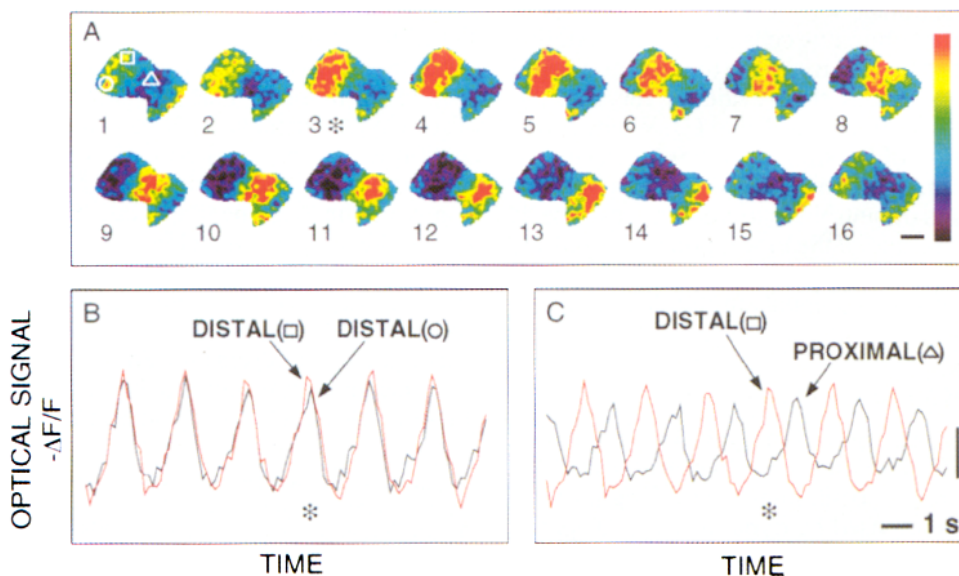


FIG. 15. Propagation of electrical waves along the lobe; posterior view (3.27.92.6s). This particular preparation shows propagation that extends into the cerebral ganglion. *A*: CCD sequence of images of activity during a single period. Parameters: 112 ms/frame,  $-\Delta F/F$  (max/min) =  $\pm 0.0015$ , scale bar = 100  $\mu\text{m}$ . *B*: optical signal  $-\Delta F/F$  vs. time for 2 locations at the distal end of the lobe but on different lateral edges; see boxes in *A*. *C*: optical signal for a location at the distal end (red) and one at the proximal end (black); see boxes in *A*. Scale bar is  $-\Delta F/F = 0.001$ . The asterisk in *B* and *C* corresponds to the time of frame 3 in *A*.

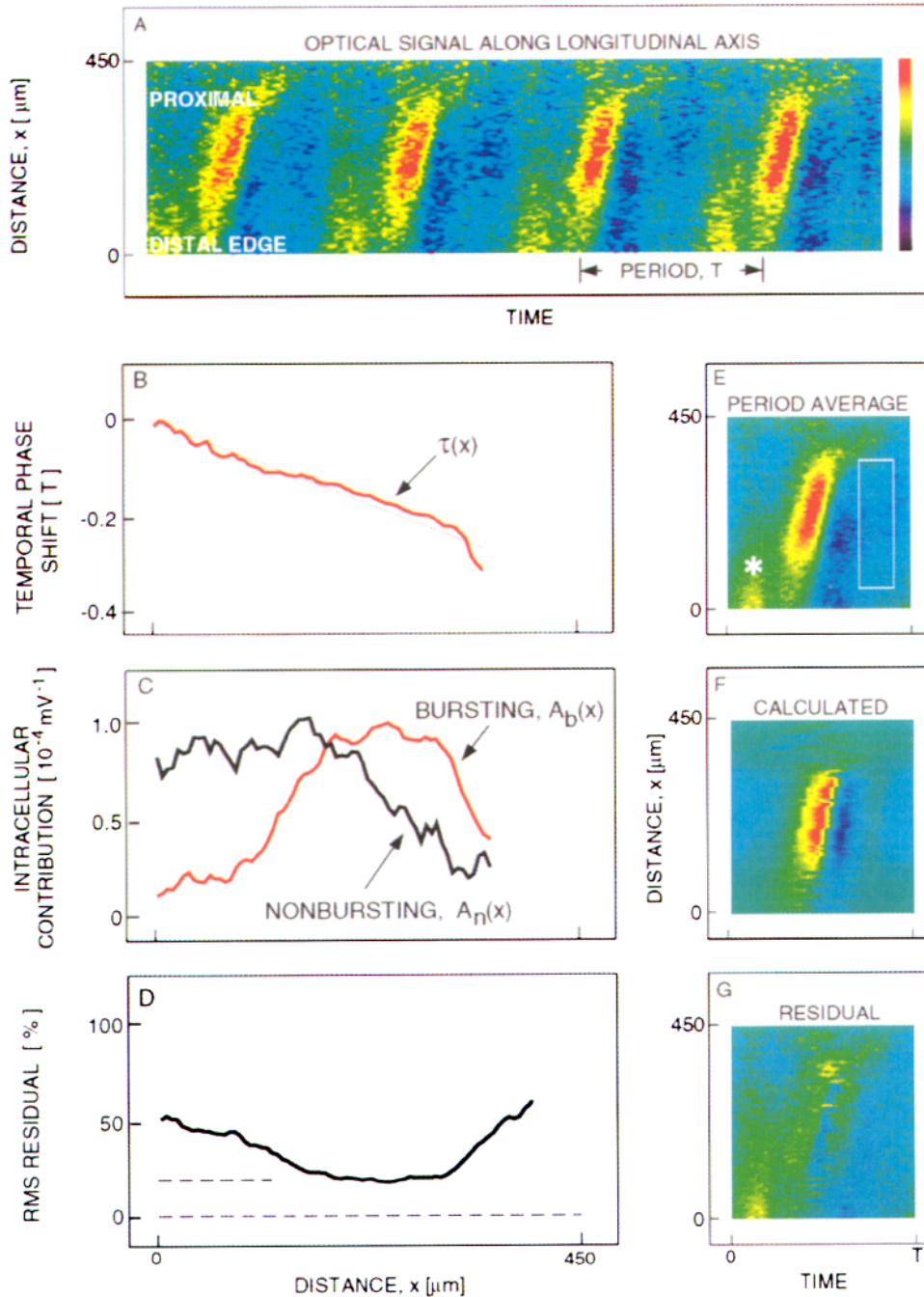


FIG. 16. Space-time analysis of electrical activity along the direction of propagation (7.13.91.4s). *A*: sequence of the electrical activity imaged along a strip coincident with the longitudinal axis of the lobe. The strip is 30 pixels wide by 100 pixels long. The data along the short axis are summed to reduce the spatial dimensions to 1. We plot activity vs. space,  $x$ , and time,  $t$ , for 4 periods. Parameters: 37 ms/frame,  $-\Delta F/F$  (max/min) =  $\pm 0.0033$ . There are 38 frames per period ( $T = 1.4$  s). *B*: the calculated phase delay  $\tau(x)$ , plotted normalized by the period,  $T$ . The thin black line has a slope of 1.1 mm/s. *C*: the calculated amplitudes  $A_b(x)$  for bursting cell contribution (red) and  $A_n(x)$  for nonbursting cells (black). *D*: the root-mean-square residual between the optical data and the fit (Eq. A5). The minimum value (dashed line) is 20%. *E*: average of the optical signal over 6 periods. Same scale as in *A*. *F*: calculated image from the fit of the intracellular records, i.e.,  $A_b(x) \Delta V_b[t + \tau(x)] + A_n(x) \Delta V_n[t + \tau(x)]$ . Same scale as in *A*. *G*: difference between the average optical signal (*D*) and the calculated fit (*E*). Same scale as in *A*.

Wave propagation is observed before, during, and after the application of low  $[\text{Cl}^-]$  saline to the preparation (Fig. 19). We observe normal wave propagation in standard saline (frames 1–7 in Fig. 19*A*), i.e., depolarization occurs

earlier at the distal versus the proximal end (Fig. 19*B*). In low  $[\text{Cl}^-]$  saline the period of oscillation is lengthened by  $\sim 50\%$ , to  $\sim 2$  s, and new patterns of electrical activity emerge (Fig. 19*C*). Often, depolarization begins at the

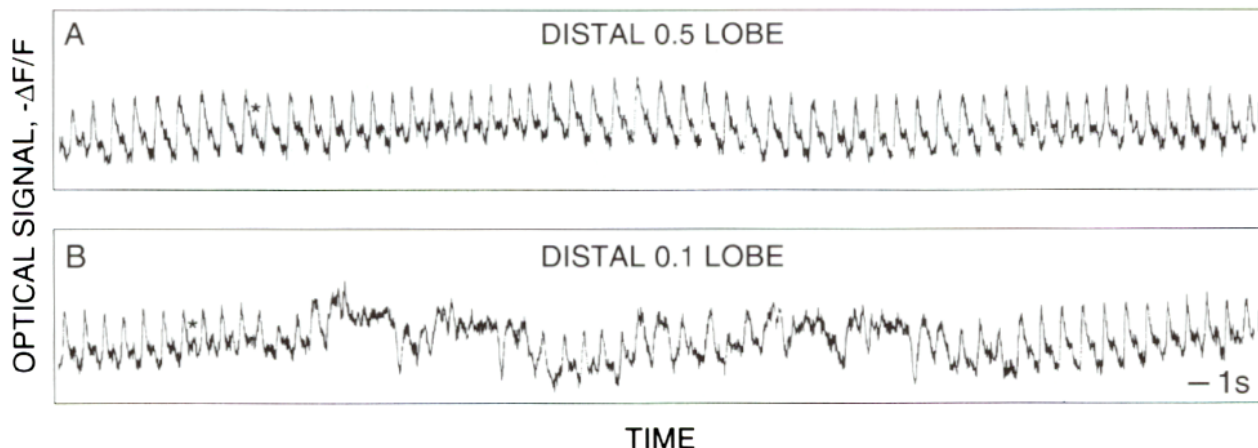


FIG. 17. Activity in a surgically reduced preparation (2.25.93). *A*: optical signal (photodiode signal  $-\Delta F/F$ ) from the distal end of the isolated distal one-half of the lobe. Note the regular rhythmicity. *B*: optical signal from the isolated distal end of the same lobe. This fragment corresponds to the site measured in *A*. It is embedded in agar to prevent motion and is only slightly larger than the beam spot ( $\sim 70 \mu\text{m}$  diam). Note the intermittent rhythmicity.

proximal end of the lobe (*frame 13* in Fig. 19*C*) and spreads distally (*frame 20* in Fig. 19*C*) until it ebbs along the distal edge (*frame 30* in Fig. 19*C*). These events correspond to a reversal of the normal wave motion, with depolarization now occurring first at the proximal versus distal end (Fig. 19*D*). The frequency of oscillation and direction of propagation returned to their original values after wash out of the

low  $[\text{Cl}^-]$  saline. Regardless of the mode of action of reducing  $[\text{Cl}^-]$ , these results demonstrate that the direction of wave propagation can reverse.

In toto, the results from the above series of experiments imply that there is a gradient of excitability along the lobe, with cells at the distal end more excitable than those at the proximal end, but that the underlying connectivity in the

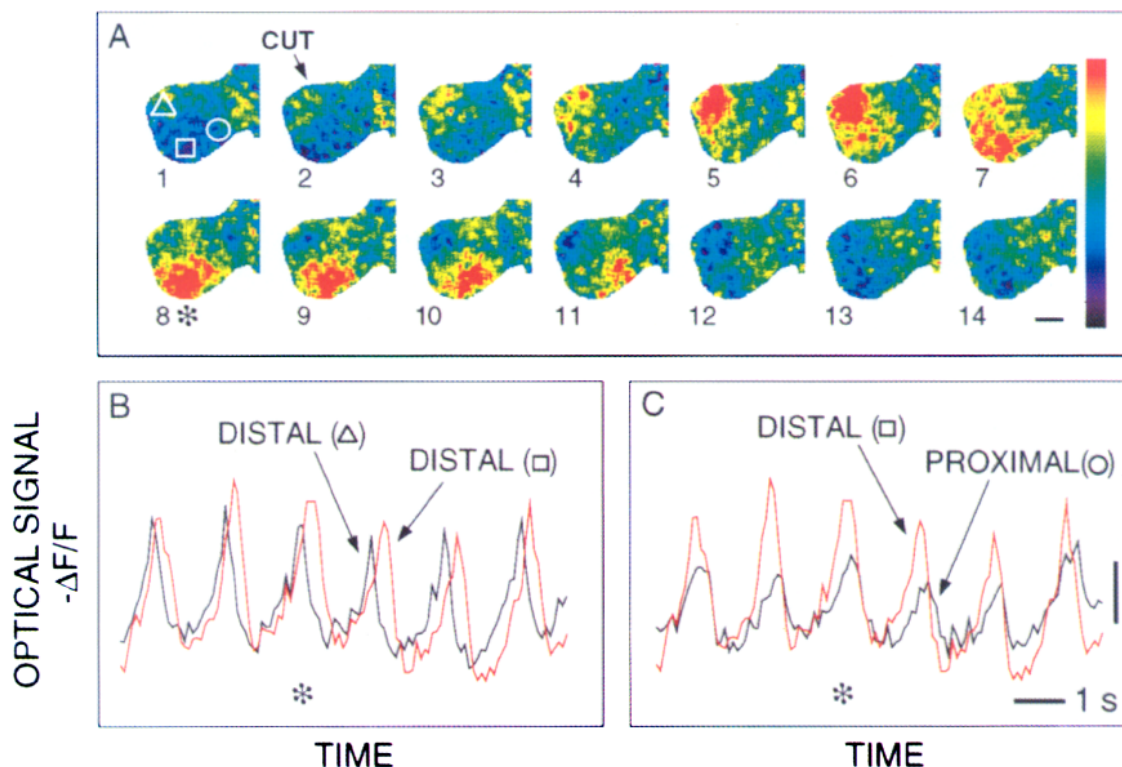


FIG. 18. Effect of a small surgical cut on the direction of propagation. The cut is along one lateral edge (see *panel 2* in *A*), perpendicular to the normal distal-proximal direction of propagation (3.20.91.7s). *A*: CCD sequence of images of activity during a single period. Parameters: 112 ms/frame,  $-\Delta F/F(\text{max/min}) = \pm 0.0015$ , scale bar =  $100 \mu\text{m}$ . *B*: optical signal  $-\Delta F/F$  vs. time for 2 locations at the distal end of the lobe but on different lateral edges (see boxes in *A*). Scale bar is  $-\Delta F/F = 0.001$ . *C*: optical signal for a location at the distal end (red) and one toward the proximal end (black; see boxes in *A*). Scale bar is  $-\Delta F/F = 0.001$ . The asterisk in *B* and *C* corresponds to the time of *frame 8*.

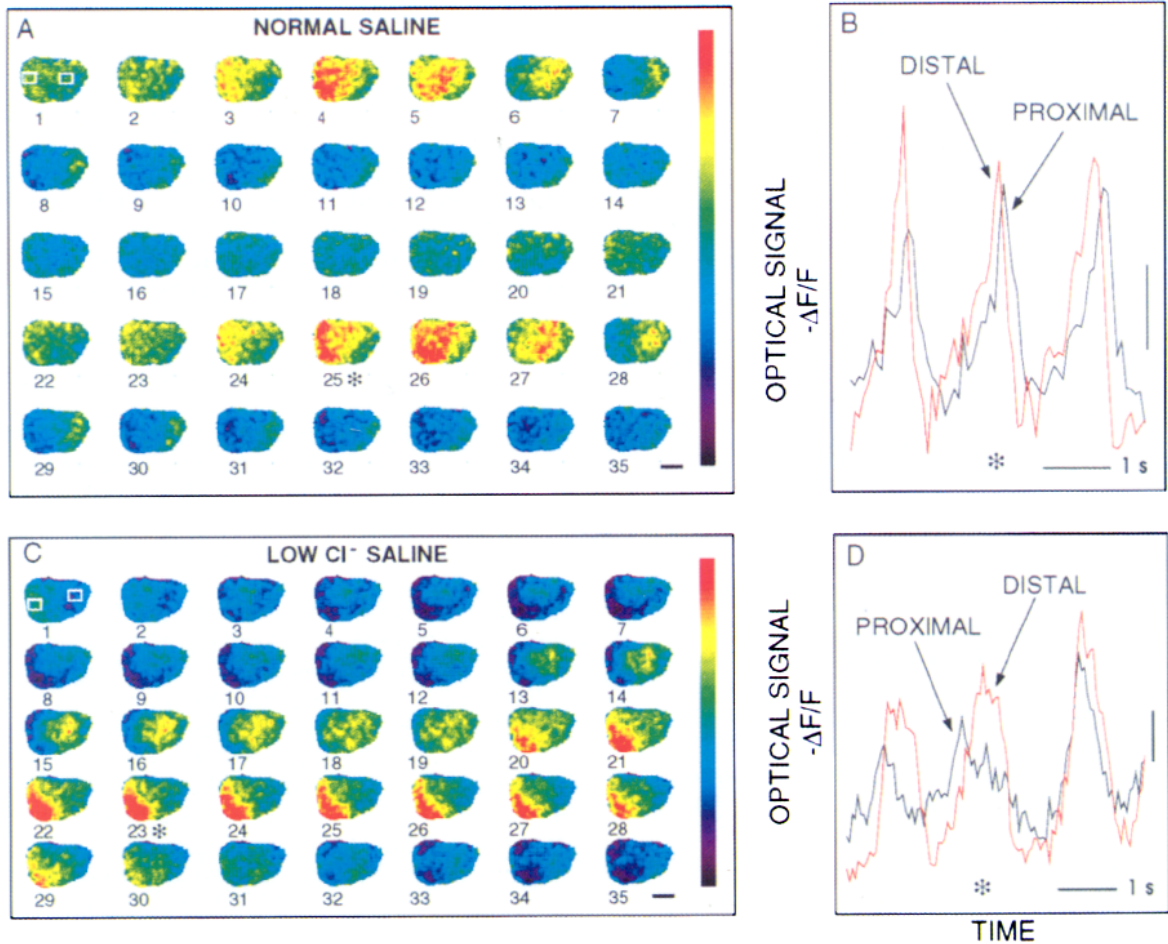


FIG. 19. Change in direction of the wave for a lobe in saline with reduced  $\text{Cl}^-$ . *A*: CCD image sequence taken in normal saline (7.15.92.3s). Parameters: 76 ms/frame,  $-\Delta F/F(\text{max/min}) = \pm 0.0032$ , scale bar = 100  $\mu\text{m}$ . *B*: optical signal  $-\Delta F/F$  vs. time for sites at the distal (red) and proximal (black) ends. Scale bar is  $-\Delta F/F = 0.001$ . The asterisk corresponds to the time of frame 25 in *A*. *C*: image sequence taken in low  $\text{Cl}^-$  saline (7.15.92.11s). Parameters: 58 ms/frame,  $-\Delta F/F(\text{max/min}) = \pm 0.0030$ , scale bar = 100  $\mu\text{m}$ . *D*: optical signal  $-\Delta F/F$  vs. time for sites at the distal (red) and proximal (black) ends. Note that electrical activity at the proximal end precedes that at the distal end, opposite from the normal direction. Scale bar is  $-\Delta F/F = 0.001$ . The asterisk corresponds to the time of frame 23 in *C*.

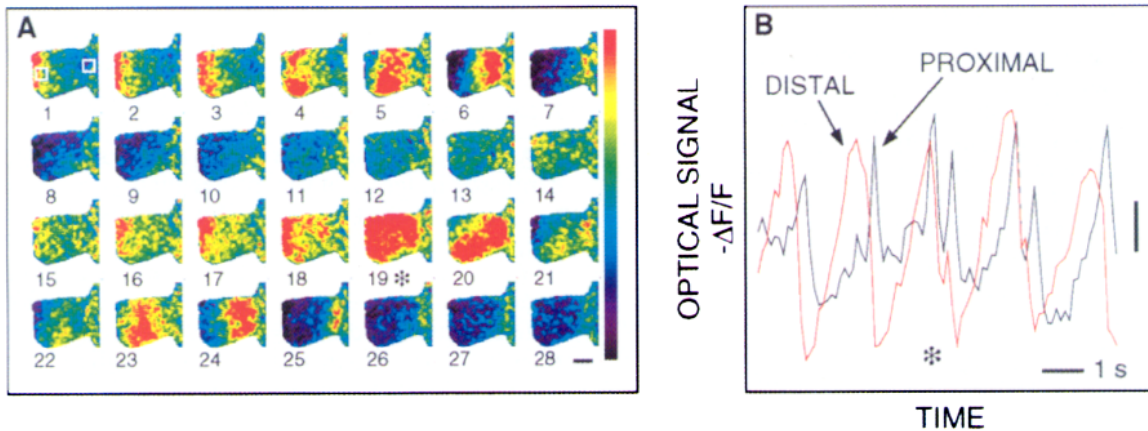


FIG. 20. Transient change in timing of activity during a double event (4.3.92.13m). *A*: image sequence at the time of a double event. Parameters: 112 ms/frame,  $-\Delta F/F(\text{max/min}) = \pm 0.0025$ , scale bar = 100  $\mu\text{m}$ . *B*: optical signal  $-\Delta F/F$  vs. time for sites at the distal (red) and proximal (black) ends. Note that electrical activity is nearly synchronous during the double event (asterisk). Scale bar is  $-\Delta F/F = 0.001$ . The asterisk corresponds to the time of frame 19 in *A*.

lobe can support the flow of electrical activity in all directions. Thus the normal direction of propagation is likely to be set by a gradient of excitability in a network with projections that run in all directions and it is not set by unidirectional connections that run distal to proximal. The extent of anisotropy in connectivity is, however, unknown.

#### *Double events and spatial synchrony*

The state with periodic, propagating waves (Figs. 14–16) is the dominant pattern of electrical behavior of the unperturbed lobe. However, as discussed in the context of the intracellular records (Figs. 6*B* and 7*B*), the rhythmic pattern of activity is occasionally interrupted by double events. We image the electrical activity of the lobe before and during these events to ascertain whether they modify the propagation of waves across the lobe. Normal propagation is observed before the double event (*frames 1–14* in Fig. 20*A*), but a transient collapse of the phase difference between the distal and proximal regions of the lobe occurs during the first of the pair of bursts (*frame 19* in Fig. 20*A*). The phase gradient is partially reestablished by the second burst (*frames 22–25* in Fig. 19*A*), after which the normal pattern of activity resumes. The detailed time dependence of the double event is shown in the plots of Fig. 20*B*.

The transient synchrony seen here (Fig. 20) occurs in isolated lobes ( $n = 5$ ) and in preparations with the nose attached ( $n = 3$ ). These data show that the lobe transiently supports a spatially uniform state in addition to the commonly observed state in which electrical activity propagates unidirectionally across the lobe.

#### DISCUSSION

We used electrical and optical methods to identify waves of electrical activity that propagate across the surface of the PC lobe of *Limax*, the central olfactory network in this animal. This approach allowed us to identify and characterize the large-scale features of the spatiotemporal dynamics and relate these dynamics to the activity of the underlying neurons.

#### *Dynamics and the underlying circuitry*

Details of the circuitry within the lobe are largely unknown, although qualitative ultrastructural examination of the lobe in a related mollusk failed to detect large numbers of synaptic contacts as defined by classical criteria<sup>8</sup> (Chase and Tolloczko 1993). Nonetheless, analogies between the dynamics reported here and theoretical understanding of excitable media (Murray 1989) allow us to draw tentative conclusions about that circuitry. 1) The phase gradient originates from a spatial gradient of excitability along the lobe. Consistent with this hypothesis is the observed tendency for surgically isolated distal ends of the lobe to oscillate faster than isolated proximal ends. 2) The direction of the spatial

gradient sets the direction of propagation. The initiation of waves near surgical cuts in a preparation (Fig. 18), which is a probable site of increased depolarization, is consistent with this assertion. 3) The magnitude of the gradient controls the phase difference along the lobe. Thus in the absence of external stimuli the gradient of excitability is such that the wavelength of the oscillating activity is roughly the size of the lobe (Figs. 14–16). 4) External stimuli and intrinsic factors modify the gradient but not necessarily the average level of excitability. Thus during double events (Fig. 20) the gradient of excitability is substantially reduced, and the wavelength becomes long compared with the size of the lobe. This results in the appearance of spatially uniform oscillations.

The lobe contains a cell-rich and a process-rich neuropil layer. Previous work shows that oscillations in LFP occur in preparations in which the complete cell layer is surgically isolated as a sheet from the neuropil layer (Gelperin et al. 1993). We now find that wave propagation in the cell layer occurs after surgical removal of the neuropil layer (unpublished results). Thus the interactions that mediate the periodic waves in the lobe are largely confined to the cell layer and its intrinsic processes.

The close correspondence between the intracellular potential recorded from a single neuron and the optical signals recorded from all of the neurons throughout the depth of the optical field (estimated to be  $\sim 10^3$  cells) suggests that the electrical activity of these cells is highly correlated (Fig. 11*A*). On the one hand, this implies that the spatial averaging inherent in our optical imaging does not lead to a significant loss of information about the neural dynamics in the lobe. On the other hand, this raises questions about the mechanism for local synchronization among these cells. Preliminary results from ultrastructural studies provide no evidence for gap-junctions between neurons in the lobe (S. Curtis, personal communication), reducing the likelihood that electrotonic coupling is responsible for the synchrony. An alternative possibility is that neurotransmission is mediated by diffuse release of transmitter. Neurons within the lobe are loaded with dense vesicles (Chase and Tolloczko 1993). These vesicles may contain classical neurotransmitters that are dispersed in a manner similar to diffuse modulatory systems.

#### *Imaging of large-scale activity*

As part of this study, we show that optical signals can be expressed in terms of the intracellular potentials of the underlying neurons (Fig. 16). This provides a spatiotemporal map of the activity of specific cell types. Our analysis builds on previous studies of the relation between optical and electrical signals. The linear dependence between dye-related optical signals and changes in intracellular potential is established for cells in invertebrate ganglia (Salzberg et al. 1973) and for cells maintained in culture (Grinvald et al. 1981). At the level of cell assemblies, Cohen and colleagues (London et al. 1987; Zecevic et al. 1989) show how optical measurements on invertebrate ganglia can be used to determine the spiking behavior of simultaneously active neurons. Similar procedures have been applied to small net-

<sup>8</sup> Chase and Tolloczko (1993) report that aggregates of presynaptic vesicles, the signature for presynaptic specialization, are prominent throughout the cell-rich layer of the lobe. However, there is no indication for widening and straightening of the intercellular space adjacent to the aggregates, the signature for synaptic contacts.

works constructed in vitro (Parsons et al. 1991). The present work demonstrates that maps of intracellular potential, and not just spiking output, can be determined for networks. Further, the present work shows that optical signals can provide unambiguous information about electrical activity in large systems, albeit not at the level of single cells. Our analytic methods should be applicable to measurements from vertebrate olfactory bulbs (Cinelli and Salzberg 1992; Kauer 1988), given the defined anatomy of this structure (Satou 1990; Shepherd and Greer 1990) and possibly other accessible areas of cortex (Grinvald et al. 1994), including olfactory cortex (Litaudon and Cattarelli 1994).

### Spatial synchrony

Large-scale spatial synchrony in the electrical activity of the PC lobe is transiently induced by the application of odorant to the nose<sup>9</sup> (Delaney et al. 1994). It is also induced by transiently increasing the concentration of nitric oxide (NO) throughout the lobe (unpublished results) with the use of photolytic methods to generate NO from a caged NO precursor (Gelperin 1994). The synchronous state in the PC lobe is likely to correspond to a global aspect of behavior, such as a change in attentiveness of the animal to its olfactory environment. Within this hypothesis, the reduction in phase that occurs during spontaneous double events in *Limax* (Fig. 20) results in spontaneous sampling of the environment and may increase the sensitivity of the animal for detecting weak olfactory stimuli. Analogous changes in global synchrony occur in visual and motor areas of mammalian cortex during periods of attention (Bouyer et al. 1981; Bressler et al. 1993; Murthy and Fetz 1992; Ribary et al. 1991).

### Conclusions

In general, processing of olfactory information depends on the physiological state of the central network at the time of sensory activation. Early measurements with mammals show that variations in the strength of “intrinsic waves” in the olfactory bulb, caused by different planes of anesthesia, dramatically influenced the effect of odor stimulation on olfactory bulb rhythms (Adrian 1950). Central olfactory networks may change their dynamical state as a function of the behavioral mode in the intact animal or as a function of the degree of anesthesia or surgical isolation in laboratory preparations. With respect to *Limax*, identified neuromodulators can alter the oscillatory activity of the isolated PC lobe for tens of minutes (Gelperin et al. 1993; Rhines 1989). Although recent measurements with intact animals (P. M. Balaban, unpublished observations<sup>10</sup>) show that the field potential of the PC lobe exhibits robust oscillations, it

is presently unknown whether these oscillations are modulated as a function of the behavioral state or in response to odor input.

### APPENDIX

Here we discuss the procedure for decomposing a space-time map (Fig. 5B) into contributions from bursting and nonbursting cells (Eq. 3). The goal is to find the optimal fit of the intracellular signal, parameterized as  $A_b(x) \Delta V_b[t + \tau(x)] + A_n(x) \Delta V_n[t + \tau(x)]$ , to the optical signal  $-\Delta F(x,t)/F(x)$ . As stated, the problem is incomplete. We thus add two constraints. First, the function  $\tau(x)$  is chosen to minimize the variance,  $\sigma^2(x)$ , at each value of  $x$ , i.e.

$$\sigma^2(x) = \left\langle \left\{ \frac{-\Delta F(x,t)}{F(x)} - A_b(x) \Delta V_b[t + \tau(x)] - A_n(x) \Delta V_n[t + \tau(x)] \right\}^2 \right\rangle_t \quad (A1)$$

where  $\langle \dots \rangle_t \equiv (1/N) \sum_{i=1}^N$  denotes averaging over time, and the functions  $A_b(x)$  and  $A_n(x)$  are given by

$$\begin{pmatrix} A_b(x) \\ A_n(x) \end{pmatrix} = \frac{1}{C_{bb}C_{nn} - C_{bn}^2} \begin{pmatrix} C_{bb} & -C_{bn} \\ -C_{bn} & C_{nn} \end{pmatrix} \times \begin{pmatrix} \left\langle \frac{-\Delta F(x,t)}{F(x)} \Delta V_b[t + \tau(x)] \right\rangle_t \\ \left\langle \frac{-\Delta F(x,t)}{F(x)} \Delta V_n[t + \tau(x)] \right\rangle_t \end{pmatrix} \quad (A2)$$

where

$$C_{bb} = \langle \Delta V_b^2(t) \rangle_t, \quad C_{nn} = \langle \Delta V_n^2(t) \rangle_t, \quad \text{and } C_{bn} = \langle \Delta V_b(t) \Delta V_n(t) \rangle_t \quad (A3)$$

Recall that  $\Delta V(t) \equiv V(t) - \langle V(t) \rangle_t$ . The second constraint is that only solutions for which the amplitudes are positive definite are valid, i.e.

$$A_b(x) \geq 0 \quad \text{and} \quad A_n(x) \geq 0 \quad \text{for all } x \quad (A4)$$

The above procedure is implemented as follows. The space-time optical records (Fig. 16A) are averaged over six cycles, as shown in Fig. 16E. The voltage data are taken from intracellular records, similar to those in Figs. 6A and 7A, averaged over six cycles in time and resampled at 27 Hz, the frame rate for the optical data (Fig. 16A). The optimal fit of the intracellular records to the optical data is found by exhaustive search for the global minimum of Eq. A1 for each value of  $x$ . The resultant functions  $\tau(x)$ ,  $A_b(t)$ , and  $A_n(t)$  are shown in Fig. 16, B and C, and used to construct Fig. 16, F and G.

An aggregate index of the goodness-of-fit of the intracellular records to the data is found by calculating the root-mean-square (RMS) residual, defined as the fractional difference between the RMS value of the optical data and that of the calculated intracellular contribution. In percent, the residual is

$$\text{RMS Residual } (x) \equiv 100 \left( 1 - \frac{\sqrt{\langle \{ A_b(x) \Delta V_b[t + \tau(x)] - A_n(x) \Delta V_n[t + \tau(x)] \}^2 \rangle_t}}{\sqrt{\left\langle \left[ \frac{\Delta F(x,t)}{F(x)} \right]^2 \right\rangle_t}} \right) \quad (A5)$$

The above equation is used to construct the plot shown in Fig. 16D.

We thank B. Friedman for preparation of histological material and for comments on an early version of this manuscript, L. B. Cohen, W. Denk,

<sup>9</sup> The concentration of odorant used in these experiments is  $\sim 10^{-4}$  M,  $\sim 10^3$  times the threshold for detection in a related mollusk (Chase 1982). It is unknown if near-threshold concentrations of odorant lead to similar changes in spatial synchrony along the lobe.

<sup>10</sup> Fine wire electrodes were inserted into the PC lobe and anchored to the sheath, as described by Balaban and Maksimova (1993). The electrical signal exhibited periodic events at 0.7 Hz, the same frequency as that observed in vitro (Gelperin and Tank 1990), along with occasional double events (e.g., Figs. 6, 7, and 20).

G. B. Ermentrout, J. J. Hopfield, N. Kopell, K. T. Moortgat, B. I. Shraiman, and H. Sompolinsky for valuable discussions and P. M. Balaban for sharing unpublished data.

D. Kleinfeld acknowledges support from the US-Israel Binational Science Foundation, Grant 90-00321/3. K. R. Delaney acknowledges support from the National Sciences and Engineering Research Council (Canada), Grant OGP0121698.

Present address of K. R. Delaney: Dept. of Biosciences, Simon Fraser University, Burnaby, BC V5A 1S6, Canada.

Address for reprint requests: D. Kleinfeld, AT&T Bell Laboratories, 600 Mountain Ave., 1C-463, Murray Hill, NJ 07974.

Received 14 January 1994; accepted in final form 22 April 1994.

## REFERENCES

- ADRIAN, E. D. Olfactory reactions in the brain of the hedgehog. *J. Physiol. Lond.* 100: 459-473, 1942.
- ADRIAN, E. D. The electrical activity of the mammalian olfactory bulb. *Electroencephalogr. Clin. Neurophysiol.* 2: 377-388, 1950.
- BALABAN, P. M. AND MAKSIMOVA, O. A. Positive and negative brain zones in the snail. *Eur. J. Neurosci.* 5: 768-774, 1993.
- BASAR, E. AND BULLOCK, T. H. (Editors). *Induced Rhythms in the Brain*. Boston, MA: Birkhäuser, 1992.
- BEURMAN, R. W. Slow potentials of the turtle olfactory bulb in response to odor stimulation of the nose. *Brain Res.* 97: 61-78, 1975.
- BOUYER, J. J., MONTARON, M. F., AND ROUGEUL, A. Fast fronto-parietal rhythms during combined focused attentive behaviour and immobility in cat: cortical and thalamic focalizations. *Electroencephalogr. Clin. Neurophysiol.* 51: 244-252, 1981.
- BRESSLER, S. L., COPPOLA, R., AND NAKAMURA, R. Episodic multiregional cortical coherence at multiple frequencies during visual task performance. *Nature Lond.* 366: 153-156, 1993.
- CATTARELLI, M. AND COHEN, L. B. Optical recording of the in vivo piriform cortex responses to electrical stimulation of the lateral olfactory tract in the rat. *Chem. Senses* 14: 577-586, 1989.
- CHASE, R. The olfactory sensitivity of snails, *Achatina fulica*. *J. Comp. Physiol. A Sens. Neural Behav. Physiol.* 148A: 225-235, 1982.
- CHASE, R. AND TOLLOCZKO, B. Interganglionic dendrites constitute an output pathway from the procerobrium of the snail *Achatina fulica*. *J. Comp. Neurol.* 283: 143-152, 1989.
- CHASE, R. AND TOLLOCZKO, B. Tracing neural pathways in snail olfaction: from the tip of the tentacles to the brain and beyond. *Micro. Res. Tech.* 24: 214-230, 1993.
- CINELLI, A. R. AND SALZBERG, B. M. Multiple site optical recording of transmembrane voltage (MSORTV), single-unit recordings, and evoked field potentials from olfactory bulb of skate (*Raja erinacea*). *J. Neurophysiol.* 64: 1767-1790, 1990.
- CINELLI, A. R. AND SALZBERG, B. M. Dendritic origin of late events in optical recordings from salamander olfactory bulb. *J. Neurophysiol.* 68: 786-806, 1992.
- DAVIS, R. H. Mushroom bodies and *Drosophila* learning. *Neuron* 11: 1-14, 1993.
- DELANEY, K. R., GELPERIN, A., FEE, M. S., FLORES, J. A., GERVAIS, R., TANK, D. W., AND KLEINFELD, D. Waves and stimulus-modulated dynamics in an oscillating olfactory network. *Proc. Natl. Acad. Sci. USA* 91: 669-673, 1994.
- DELANEY, K. R., KLEINFELD, D., AND TANK, D. W. CCD-imaging of voltage sensitive dye signals from whole brain of lower vertebrates. *Soc. Neurosci. Abstr.* 18: 967, 1992.
- DÖVING, K. B. The influence of olfactory stimuli upon the activity of secondary neurons in the burbot (*Lota lota L.*) *Acta Physiol. Scand.* 66: 290-299, 1966.
- ECKHORN, R., BAUER, R., JORDAN, W., BROSCHE, M., KRUSE, W., MUNK, M., AND REIBOECK, R. J. Coherent oscillations: a mechanism of feature linking in the visual system? Multiple electrode and correlation analysis in the cat. *Biol. Cybern.* 60: 121, 1988.
- FEE, M. S., DELANEY, K. R., GELPERIN, A., STEPANOSKI, R. A., TANK, D. W., AND KLEINFELD, D. Spatiotemporal variations in the activity of an oscillatory neuronal network in the terrestrial mollusc *Limax* (Abstract). *Biophys. J.* 1992.
- FREEMAN, W. J. *Mass Action in the Brain*. New York: Academic, 1975.
- FREEMAN, W. J. Spatial properties of an EEG event in the olfactory bulb and cortex. *Electroencephalogr. Clin. Neurophysiol.* 44: 586-605, 1978.
- GELPERIN, A. Olfactory basis of homing behavior in the giant garden slug, *Limax maximus*. *Proc. Natl. Acad. Sci. USA* 71: 966-970, 1974.
- GELPERIN, A. Nitric oxide mediates network oscillations of olfactory interneurons in a terrestrial mollusc. *Nature Lond.* 369: 61-63, 1994.
- GELPERIN, A., GERVAIS, R., DELANEY, K. R., FEE, M. S., FLORES, J., TANK, D. W., AND KLEINFELD, D. Olfactory interneuron oscillations: optical and electrical measurements of intrinsic and odor-modulated activity. *Soc. Neurosci. Abstr.* 18: 303, 1992.
- GELPERIN, A., RHINES, L. D., FLORES, J., AND TANK, D. W. Coherent network oscillations by olfactory interneurons: modulation by endogenous amines. *J. Neurophysiol.* 69: 1930-1939, 1993.
- GELPERIN, A. AND TANK, D. W. Odour-modulated collective network oscillations of olfactory interneurons in a terrestrial mollusc. *Nature Lond.* 435: 437-440, 1990.
- GERARD, R. W. AND YOUNG, J. Z. Electrical activity of the central nervous system of the frog. *Proc. R. Soc. Lond. B Biol. Sci.* B122: 343-352, 1937.
- GRAY, C. M., KONIG, P., ENGEL, A. K., AND SINGER, W. Oscillatory responses in cat visual cortex exhibit intercolumnar synchronization which reflects global stimulus properties. *Nature Lond.* 338: 334-337, 1989.
- GRINVALD, A., FROSTIG, R. D., LIEKE, E., AND HILDESHEIM, R. Optical imaging of neuronal activity. *Physiol. Rev.* 68: 1285-1366, 1988.
- GRINVALD, A., LIEKE, E. E., FROSTIG, R. D., AND HILDESHEIM, R. Cortical point-spread function and long-range lateral interactions revealed by real-time optical imaging of macaque monkey primary visual cortex. *J. Neurosci.* 14: 2545-2568, 1994.
- GRINVALD, A., ROSS, W. N., AND FARBER, I. C. Simultaneous optical measurements of electrical activity from multiple sites on the processes of cultured neurons. *Proc. Natl. Acad. Sci. USA* 78: 3245-3249, 1981.
- GUCKENHEIMER, J. AND HOLMES, P. *Nonlinear Oscillations, Dynamic Systems and Bifurcations of Vector Fields*. New York: Springer, 1983.
- HORN, R. AND MARTY, A. Muscarinic activation of ionic currents measured by a new whole cell recording method. *J. Gen. Physiol.* 92: 145-159, 1988.
- KAUER, J. S. Real-time imaging of evoked activity in local circuits of the salamander olfactory bulb. *Nature Lond.* 331: 166-168, 1988.
- KAUER, J. S., SENSEMAN, D., AND COHEN, L. B. Odor elicited activity monitored simultaneously from 124 regions of the salamander olfactory bulb using a voltage sensitive dye. *Brain Res.* 418: 255-261, 1987.
- KETCHUM, K. L. AND HABERLY, L. B. In: *Olfaction: A Model System for Computational Neuroscience*, edited by J. L. Davis and H. Eichenbaum. Cambridge, MA: MIT Press, 1991, p. 69-100.
- KITTEL, R. Untersuchungen über dens Geruchs- und Geschmackssinn bei den Gattungen *Arion* und *Limax*. *Zool. Anz.* 157: 185-195, 1956.
- LASSER-ROSS, N., MIYAKAWA, H., LEV-RAM, V., YOUNG, S. R., AND ROSS, W. N. High time resolution fluorescence imaging with a CCD camera. *J. Neurosci. Methods* 26: 253-261, 1991.
- LAURENT, G. AND NARAGHI, M. Odorant-induced oscillations in the mushroom bodies of the locust. *J. Neurosci.* 14: 2993-3004, 1994.
- LITAUDON, P. AND CATTARELLI, M. Multi-site optical recording of the rat piriform cortex activity. *NeuroReport* 5: 743-746, 1994.
- LOEW, L. M., COHEN, L. B., DIX, J., FLUHLER, E. N., MONTANA, V., SALAMA, G., AND WU, J.-Y. A naphthyl analog of the aminostyryl pyridinium class of potentiometric membrane dyes shows consistent sensitivity in a variety of tissue, cell and model membrane preparations. *J. Membr. Biol.* 130: 1-10, 1992.
- LONDON, J. A., ZECEVIC, D., AND COHEN, L. B. Simultaneous optical recording from many neurons during feeding in *Navanax*. *J. Neurosci.* 7: 649-661, 1987.
- MOONEY, R. AND WAZIRI, R. Agarose gels stabilize isolated molluscan neurons for long-term recording. *J. Neurosci. Methods* 5: 249-251, 1982.
- MURRAY, J. D. *Mathematical Biology*. Berlin: Springer Verlag, 1989.
- MURTHY, V. N. AND FETZ, E. E. Coherent 25- to 35-Hz oscillations in the sensorimotor cortex of awake behaving monkeys. *Proc. Natl. Acad. Sci. USA* 89: 5670-5674, 1992.
- ORBACH, H. S. AND COHEN, L. B. Optical monitoring of activity from many areas of the in vitro and in vivo salamander olfactory bulb: a new method for studying functional organization in the vertebrate central nervous system. *J. Neurosci.* 3: 2251-2262, 1983.
- PARSONS, T. D., SALZBERG, B. M., OBAID, A. L., RACCUA-BEHLING, F., AND KLEINFELD, D. Long-term optical recording of electrical activity in

- ensembles of cultured *Aplysia* neurons. *J. Neurophysiol.* 66: 316–333, 1991.
- RHINES, L. D. *Physiology and Pharmacology in the Procerebrum of Limax maximus* (Senior thesis). Princeton, NJ: Princeton Univ., 1989.
- RIBARY, U., IOANNIDES, A. A., SINGH, K. D., HANSON, R., BOLTON, J. P. R., LADO, F., MOGILNER, A., AND LLINAS, R. Magnetic field tomography of coherent thalamocortical 40-Hz oscillations in humans. *Proc. Natl. Acad. Sci. USA* 88: 11037–11041, 1991.
- ROSS, W. N. AND REICHARDT, L. B. Species-specific effects on the optical signals of voltage-sensitive dyes. *J. Membr. Biol.* 48: 343–356, 1979.
- SAHLEY, C. L., MARTIN, K. A., AND GELPERIN, A. Odors can induce feeding motor responses in the terrestrial mollusc *Limax maximus*. *Behav. Neurosci.* 106: 563–568, 1992.
- SALZBERG, B. M., DAVILA, H. V., AND COHEN, L. B. Optical recording of impulses of an invertebrate central nervous system. *Nature Lond.* 246: 508–509, 1973.
- SATOU, M. Synaptic organization, local neuronal circuitry, and functional segregation of the teleost olfactory bulb. *Prog. Neurobiol.* 34: 115–142, 1990.
- SCHILD, D. *Chemosensory Information Processing*. Berlin: Springer-Verlag, 1990.
- SCHUSTER, H. G. (Editor). *Nonlinear Dynamics and Neuronal Networks: Proceedings of the Sixty-Third W. E. Heraeus Seminar, Friedrichsdorf 1990*. New York: VCH, 1991.
- SCHÜTT, A. AND BAŞAR, E. Olfactory field potential oscillations in the isolated *Helix* brain: different odors induce different rhythmicities (Abstract). *Proceedings of the 39th Annual Meeting of the German Electroencephalography Society*, 1994.
- SHEPHERD, G. M. AND GREER, C. A. Olfactory bulb. In: *The Synaptic Organization of the Brain* (3rd ed.), edited by G. M. Shepherd. New York: Oxford Univ. Press, 1990, p. 133–169.
- VERATTI, E. Ricerche sul sistema nervoso dei *Limax*. *Reala Inst. Lomb. Sci. Let. Mem.* 18: 163–179, 1900.
- WIELAND, S. J. AND GELPERIN, A. Dopamine elicits feeding motor program in *Limax maximus*. *J. Neurosci.* 3: 1735–1745, 1983.
- YAMADA, A., SEKIGUCHI, T., SUZUKI, H., AND MIZUKAMI, A. Behavioral analysis of internal memory states using cooling-induced retrograde amnesia in *Limax flavus*. *J. Neurosci.* 12: 729–735, 1992.
- ZECEVIC, D., WU, J.-Y., COHEN, L. B., LONDON, J. A., HOPP, N.-P., AND FALK, C. X. Hundreds of neurons in the *Aplysia* abdominal ganglion are active during the gill-withdrawal reflex. *J. Neurosci.* 7: 3681–3689, 1989.